nature biomedical engineering

Article

https://doi.org/10.1038/s41551-026-01681-z

4D-printed adaptive hydrogel tissue expanders for ear and breast reconstruction

Received: 26 January 2024

Accepted: 13 April 2026

Published online: 01 June 2026

Check for updates

Di Wang[1,2,6], Jia-Qi Lü[3,4,6], Xiao Kuang[2,5,6], Liming Lian[2], Sili Yi[2], Hossein Ravanbakhsh[2], Jin-Song Li[3,4], Guosheng Tang[2], Maobin Xie[2], Carlos Ezio Garciamendez-Mijares[2], Prajwal Agrawal[2], Zixuan Wang[2], Sushila Maharjan[2], Wen Chen[1], Haiyue Jiang[1,7] ✉ & Yu Shrike Zhang[2,7] ✉

Tissue expanders are widely used for organ and tissue reconstruction surgery. Hydrogel tissue expanders that swell in a biofluid are promising for minimally invasive operations. Nevertheless, clinical applications of existing hydrogel tissue expanders exhibit simple geometries, rapid swelling and insufficient mechanical performances. Here we develop a negatively charged polyelectrolyte hydrogel ink for light-based printing and prolonged yet large expansive profiles for surface organ and tissue reconstruction. This 4D-printed hydrogel tissue expander can be moulded in architecturally sophisticated constructs that adapt to the environment and show favourable mechanics without the need of external triggers for expansion. The ionization degree of the polyelectrolyte hydrogels is tunable by pH value in the surrounding medium and allows a volume equilibrium–swelling up to 10–30 times. In a rabbit model, we use the tissue expander for reconstruction of human-size ears and breasts, highlighting their multifold advantages over existing clinically adopted methods and thus future translation potentials.

Reconstruction of congenital and acquired body surface organ malformations, including the absence of external auricle, nose and eyelid, as well as large surface defects generated from the removal of scars and keloids, giant nevi and tumours, is the major duty for reconstruction surgeons where tremendous numbers of patients are waiting for treatments[1–6]. To this end, tissue expansion as an emerging strategy has opened a new era in the field of organ and tissue reconstruction surgery and has hence become indispensible[7]. The insertion and expansion of a tissue expander, oftentimes under the skin, allow delayed prefabrication of the covering tissue to increase its area or amount and improve the vascularization and blood supply of the local flap, thus helping the surgeon to obtain a larger flap for reconstruction elsewhere on the same patient[8,9]. Gradually, the expanded tissue expander introduces continual forces that stretch the skin tissue surrounding the expander[10]. Responses to biomechanical forces, biological systems, from the microscale genes, cells and extracellular matrix to the macroscale skin tissue, participate in balancing the local forces by imposing a viscoelastic resistance through mechanotransduction across the spatiotemporal scales, eventually leading to the increase in both epidermal and dermal areas[11,12]. Taking advantage of an expanded local skin flap will help to collect the tissue with similar colour, texture and sensation to the tissue of the recipient site, achieve better aesthetic results in addition to functional reconstruction, reduce the possibility of complications in the donor area and improve surgical outcomes[13,14].

[1]Plastic Surgery Hospital of Chinese Academy of Medical Sciences & Peking Union Medical College, Beijing, People's Republic of China. [2]Division of Engineering in Medicine, Department of Medicine, Brigham and Women's Hospital, Harvard Medical School, Cambridge, MA, USA. [3]Center for Advanced Laser Technology, Hebei University of Technology, Tianjin, People's Republic of China. [4]Hebei Key Laboratory of Advanced Laser Technology and Equipment, Tianjin, People's Republic of China. [5]Department of Mechanical Engineering, University of Wisconsin-Madison, Madison, WI, USA. [6]These authors contributed equally: Di Wang, Jia-Qi Lü, Xiao Kuang. [7]These authors jointly supervised this work: Yu Shrike Zhang, Haiyue Jiang. ✉e-mail: jianghaiyue@psh.pumc.edu.cn; yszhang@bwh.harvard.edu

Over the years with technological evolution, there have been multiple iterations of tissue expanders, from the initial inflatable rubber devices to the more recently demonstrated self-expansion hydrogels in arbitrary shapes[15–19]. Nevertheless, all clinically used internally buried rubber tissue expanders require injections of normal saline from outside the body through an injection port and repeated needle punctures penetrating the skin during the expansion process. These procedures are challenging owing to the lack of compliance and cooperation of many patients, especially children under age 12, who fear the pain caused by repeated punctures[20]. Besides, repeated needle punctures also notably increase the risks of rupture and deflation[15].

For these reasons, the self-expanding hydrogel tissue expanders that can swell by directly absorbing the surrounding biofluids offer a potential solution to tackle such issues. Different hydrogel systems of self-expanding tissue expanders have been developed and applied towards reconstruction surgery. In some earlier works, hydrogels based on a copolymer of *N*-vinyl-2-pyrrolidone and methylmethacrylate (NVP–MMA) were explored to produce tissue expander devices, which could quickly swell when fully absorbed with physiological media[18,21,22]. Other materials, including poly(styrene-maleic anhydride) and poly(ethylene glycol)-diacrylate (PEGDA) hydrogels, have also been used for producing self-expanding hydrogel tissue expanders with adjustable swelling ratios and mechanical properties[19,23]. Nevertheless, there still is a long-lasting conflict between the large swelling and the mechanical toughness. Hydrogels with loose crosslinking facilitate extensive swelling while eliciting weak mechanical properties. As a result, the substantial reduction in stiffness and mechanical strength after equilibrium swelling would provide insufficient resistance to skin tension making it hard to meet clinical requirements such as in the abovementioned examples.

To this end, various tough hydrogels by polymer network designs, including double-network hydrogels[24,25], highly entangled hydrogels[26] and phase-separated composite hydrogels[27,28], have been developed to achieve favourable mechanical properties, including toughness and fatigue resistance. However, the dense polymer networks substantially restrict hydrogel swelling (swelling ratio of usually <3)[26]. More importantly, these conventional hydrogels intrinsically show a one-step swelling behaviour due to water diffusion driven by the mixing thermodynamics, consequently exhibiting fast yet highly limited control over their expansion profiles. This problem essentially blocks their applications in tissue expanders because the aggressive expansion will exert high tensions on the skin tissue and thus extreme discomfort (for example, pains) to the patients. All these challenges hinder the development of advanced hydrogel tissue expanders with large, prolonged swelling while in the meantime retaining good mechanics to accommodate satisfactory clinical outcomes.

In this Article, we report the development of environmentally adaptive, highly expandable and biocompatible hydrogels for four-dimensional (4D) printing of shape-customizable tissue expanders (Fig. 1a). We meticulously designed polyelectrolyte hydrogels with environment-dependent equilibrium swelling capability for 4D printing of the tissue expanders, termed the adaptive-expansion hydrogel tissue expanders (AEH-TEs). The polyelectrolyte hydrogels with tunable chemical crosslinking contain numerous entanglements (physical crosslinking) at high precursor concentrations, enabling both large swelling and favourable mechanical performances[26]. The swelling of AEH-TEs is controlled by coupled water and electrolytes diffusion, exhibiting unique environmentally adaptive, large and prolonged swelling capability. Their ionization degrees dynamically change by altering the medium pH value in vitro or absorbing the small-molecule electrolytes from body fluids in vivo in clinical settings. We established an experimentally validated synthesis–swelling model based on the swelling theory and numerical analyses considering the critical role of crosslinking density and the degree of ionization. The model enables predicting the equilibrium swelling ratios and stiffness of the polyelectrolyte hydrogels for various material formulations at broad ionization degree conditions.

Compared with conventional hydrogel tissue expanders, our AEH-TEs simultaneously exhibit unique prolonged and large swelling while maintaining favourable mechanical properties (Fig. 1b). We showcased the 4D printing of single-material constructs with isotropic self-expansion and multi-material ones with anisotropic self-expansion capabilities. We further demonstrated the translational potential of the printed ear-shaped and breast-shaped AEH-TEs for ear and breast reconstruction, respectively. In vivo tests revealed that the printed tissue expander devices using the selected formulation suitable for this intended application could gradually swell beyond 10 times in volume without the need for external fluid injection, yet still favourably maintained structural and mechanical integrity during deformation under the rabbit skin. Two weeks after implantation, the devices helped to expand the covering skin tissues exactly in the intended shapes and facilitated neoangiogenesis of the expanded flap, unlike the considerable complications associated with the control group where current clinical-standard repeated injection-based rubber tissue expanders were used, suggesting promise for future clinical translations. No systemic immune-inflammatory responses were observed.

Results and discussion

Design of AEHs

To realize prolonged, large swelling for hydrogel tissue expanders, we designed polyelectrolyte hydrogels with extensive degrees of entanglements and pH-dependent equilibrium swelling capability. As a proof of concept, we synthesized high-concentration poly(acrylic acid) (PAA) hydrogels (50.0%, *w*/*w* unless otherwise noted) with low contents of PEGDA crosslinkers by radical photopolymerization (detailed resin formulations are provided in Supplementary Table 1). PAA has been widely used in drug delivery and tissue engineering owing to its biocompatibility[29,30]. In addition, PEGDA has been approved by the US Food and Drug Administration for certain in vivo applications[31]. A series of PAA hydrogels with precisely controlled ionization degrees were fabricated through partially neutralized acrylic acid (AA) molecules with sodium hydroxide (NaOH) to produce sodium acrylic acid (AANa), that is, the –COOH in AA turning to $–COO^-$ by deprotonation with Na^+ as the counter ion. The hydrogel precursors were photocrosslinked in the presence of diphenyl(2, 4, 6-trimethylbenzoyl)phosphine oxide (TPO) as the photoinitiator. The inks were loaded into a digital light processing (DLP) printer to fabricate three-dimensional (3D) constructs using optimized printing parameters (Fig. 1a and Supplementary Table 2). After printing, the 3D constructs were immersed in normal saline for swelling (Supplementary Video 1). The finite element simulation shows that the human ear model (with a degree of ionization (α) of 0.4) swells and reaches a stable volume in 72 h (Supplementary Video 2). Also, the prolonged swelling does not induce any distortion to the original geometry, leading to a suitable property for using the construct as a tissue expander compared to the conventional ultrafast swelling that features also weak mechanics (Fig. 1b).

The swelling ratio was experimentally determined by the mass ratio of the swollen hydrogel, after reaching swelling equilibrium, to the as-printed one. It was found that the initiator concentration mainly affected the photopolymerization rate while showing a small influence on the final equilibrium ratio (Supplementary Fig. 1). Although the 0.5% TPO hydrogel exhibited a marginally higher swelling ratio compared to the 0.1% group, its polymerization reaction was less controllable, as the reaction became overly vigorous with excessive heat generation, potentially resulting in printing failure. When the initiator content was high (>2.0%), the reaction was extremely violent and exothermic, which produced plenty of bubbles. Therefore, 0.1% TPO, which could initiate appropriate polymerization of hydrogels with a sufficient swelling ratio to meet clinical requirements, was selected and used in the rest of the experiments. Additionally, the hydrogel-precursor

https://doi.org/10.1038/s41551-026-01681-z

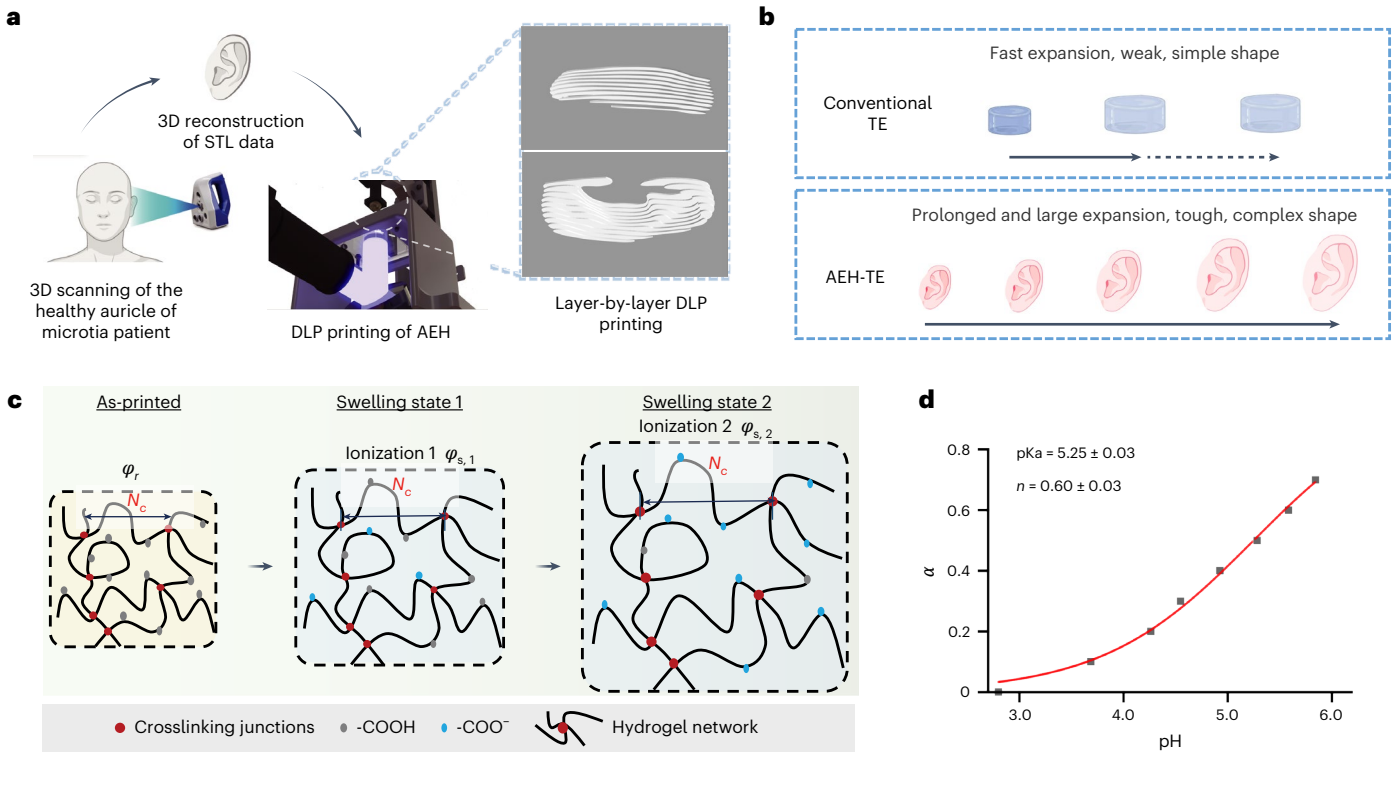

Fig. 1 | Design and mechanism of AEHs. a, Scheme and workflow of DLP printing of an ear-shaped AEH-TE: a personalized digital ear model is first created by 3D scanning and then sliced into layered images to feed the DLP printer to produce the physical construct via layer-by-layer photocrosslinking. **b**, Scheme showing the expansion behaviours of conventional tissue expanders with fast and oftentimes small expansion, as well as our designed AEH-TEs with prolonged and relatively large expansion. **c**, Scheme showing the polymer-network structures of AEH-TE at different expansion stages: as-printed and equilibrium swelling at two different ionization degree (α) values. **d**, Degree of ionization (α) of PAA-based AEHs as a function of pH value. Experiment, solid mark; model fitting, dashed line. pKa, acid dissociation constant; n, Hill coefficient. **e**, Photographs showing printed pyramid-shaped AEHs at different expansion stages: as-printed and equilibrium swelling at three different α values as labelled. Swelling tests were performed in normal saline. Scale bars, 1 cm. Schematics created in BioRender; **a**, Wang, D. https://BioRender.com/2sifq7t (2026); **b**, Wang, D. https://BioRender.com/kzylxh6 (2026).

concentration of 50.0% provided a faster photopolymerization rate than that of 25.0% and a comparably large equilibrium swelling ratio of 70.0% (Supplementary Fig. 2). Thus, PAA hydrogel precursor of 50.0% was used for the rest of study.

The swelling ratios and mechanical properties of the polyelectrolyte hydrogels can be tuned by altering the ink formation, including monomer and crosslinker contents and crosslinker molecular weight. Moreover, α of the negatively charged carboxylic groups in the hydrogel network is enhanced by increasing the medium pH value (Supplementary equation (7)), enabling environmentally adaptive equilibrium swelling capability and stiffness. We accordingly developed a modified synthesis–swelling model to investigate the relations between the swelling behaviours and the mechanical properties of the AEH polymer networks. After crosslinking of the hydrogel precursor (volume fraction, φ_0), it can be assumed that the polymer chains take a relaxed state at Gaussian configuration, which is thus used as the reference state (volume fraction, $\varphi_r = \varphi_0$) (Supplementary Text and Supplementary Table 3). The hydrogels quickly absorb the water molecules upon soaking in the buffer, reaching equilibrium swelling (volume fraction φ_s) (Fig. 1c). The swelling ratio is therefore determined with reference to the relaxed state ($Q = \varphi_r/\varphi_s$). The hydrogel swelling is a water-diffusion process driven by the water osmotic pressure in the hydrogel network, described by the mean-field Flory–Rehner equation and its derived predictive models[32,33]. The osmotic pressure contributed by mixing, network deformation and Donnan equilibrium reaches zero at the swelling equilibrium state (Supplementary equation (14))[34]. Q of a given PAA hydrogel can be analytically resolved to be associated with network chain length (N_c) and effective Flory–Hugging's interaction parameter (χ_{eff}) in salt solution (Supplementary equation (18)). In addition, the swelling theory shows that the shear modulus (G_s) is determined by the initial concentration (φ_r), structure parameter (N_c) and swelling state (φ_s) in a swollen hydrogel (Supplementary equation (23)). The rise in α enhances the affinity between the water molecule and the polymer network, leading to higher swelling capability. In PAA-based AEHs, the change of environmental pH value and the supply of electrolytes would result

https://doi.org/10.1038/s41551-026-01681-z

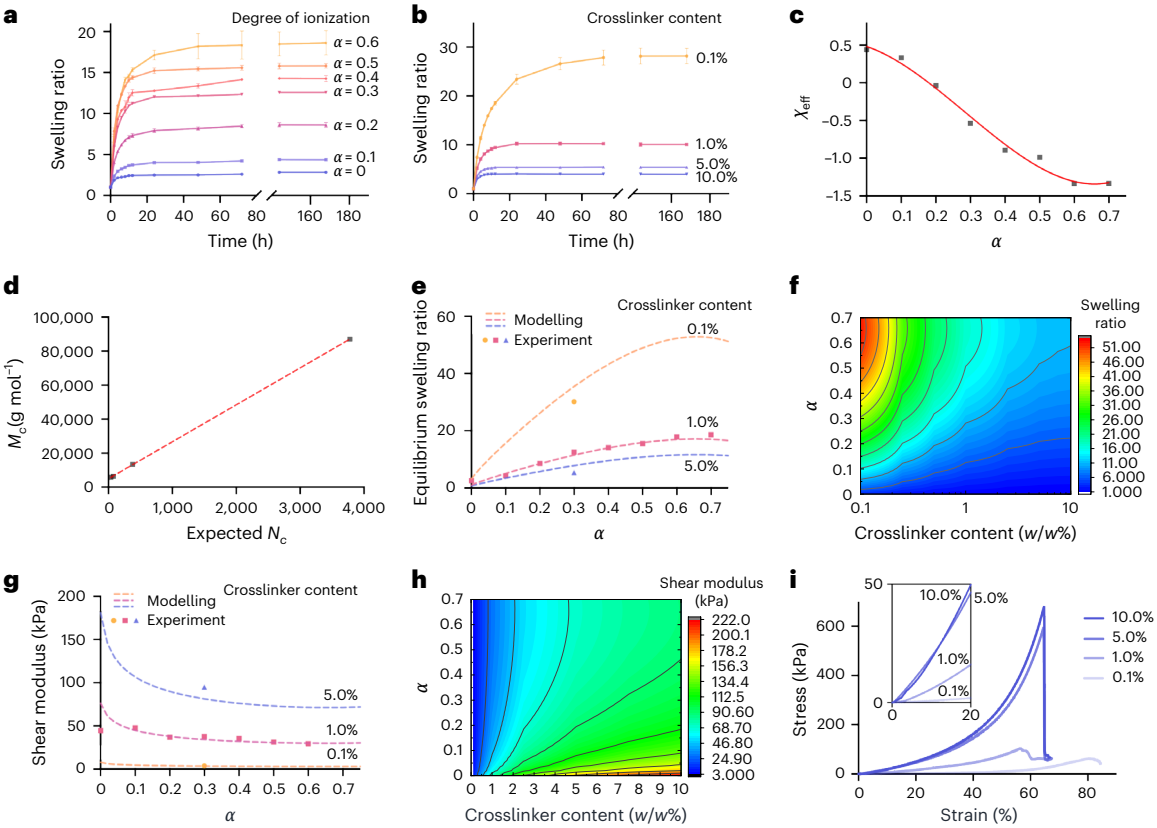

Fig. 2 | Synthesis–swelling relation and mechanical properties of AEHs. **a**,**b**, Mass swelling ratio as a function of swelling time for PAA-based AEHs with different synthesis formulations: AEHs with different initial ionization degrees (α) from 0 to 0.6 (mean ± s.d., $n = 4$ biological replicates) (**a**), and AEHs with different PEGDA-1000 ($M_w = 1{,}000$ g mol^{-1}) crosslinker contents from 0.1% to 10.0% (mean ± s.d., $n = 4$ biological replicates) (**b**). **c**, Calculated Flory–Hugging's interaction parameter (χ_{eff}) as a function of α. **d**, Linear correlation between the calculated network-chain molecular weight (M_c) and the expected network chain length (N_c). **e**, Experimental and predicted equilibrium swelling ratios as a function of α for AEHs consisting of different contents of crosslinker from 0.1% to 5.0% as labelled. **f**, Colour contour showing the equilibrium swelling ratio as a function of both crosslinker content (0.1–10.0%) and α (0–0.7). **g**, Experimental and predicted equilibrium shear moduli as a function of α for AEHs consisting of different contents of crosslinker from 0.1% to 5.0% as labelled. **h**, Colour contour showing the equilibrium shear modulus of AEHs as a function of crosslinker content (0.1–10.0%) and α (0–0.7). **i**, Compression stress–strain curves of AEHs consisting of different crosslinker contents as labelled after swelling equilibrium. All swelling tests were performed in normal saline.

in the increase in α because of the enhanced ionization of –COOH to –COO$^-$ groups (Fig. 1d). As an example, the environmentally adaptive swelling behaviour was illustrated by the printed pyramids (Fig. 1e), exhibiting increased swollen sizes (or equilibrium swelling ratios) for hydrogels at higher α.

Synthesis–swelling relation and mechanical properties

We investigated the swelling behaviours and mechanical properties of AEHs through both experiments and modelling. We first experimentally investigated the α-dependent swelling behaviours of AEH with 1.0% PEGDA-1000 (molecular weight $M_w = 1{,}000$ g mol^{-1}) crosslinker. The neutralization of AA by NaOH in the precursors enabled quantitatively increased α value of the obtained hydrogels, exhibiting enhanced equilibrium swelling ratios. The hydrogels without alkaline treatment ($\alpha \approx 0$) showed a small swelling ratio of 2.6 ± 0.07 (Fig. 2a). The increase in α (from 0.1 to 0.6, that is, NaOH/AA molar ratio of 0.1 to 0.6) resulted in notably enhanced equilibrium swelling ratio from 4.1 ± 0.1 to 19.0 ± 1.5. With $\alpha > 0.3$, the hydrogels showed an increasing swollen size with prolonged soaking time and reached an equilibrium swelling ratio of over 10 after 24 h. The compression tests revealed that the mechanical properties decayed with increasing α, because the network chains gradually elongated and became segregated by the large amount of water molecules. Despite the weakened intermolecular interactions by swelling, the reversible sliding and recovery of the stretched network chains by molecular entanglements could enable favourable mechanical strengths even at high swelling[35]. Accordingly, the hydrogels at a high α of 0.6 still exhibited a high compressive modulus of 87.6 ± 5.0 kPa and break strain of over 40% after swelling to 18-fold of initial size (Supplementary Fig. 3).

We further studied the influence of PEGDA-1000 crosslinker content on the swelling behaviours. With the increase in crosslinker concentration from 0.1% to 10.0%, the swelling ratio markedly reduced from 29.3 ± 1.3 to 4.0 ± 0.3 (Fig. 2b). The compressive moduli and strengths dropped from 360.99 ± 23.84 kPa to 112.53 ± 1.61 kPa, and from 510.21 ± 101.17 kPa to 129.10 ± 44.67 kPa, respectively (Supplementary Fig. 4). The failure strains of hydrogels with higher crosslinker concentrations (1.0–10.0%) were close to each other but increased to over 80% at a low PEGDA crosslinker content of 0.1%. This observation could be attributed to the molecular entanglement outnumbering the chemical crosslinks at the very low crosslinker content[35], leading to increased toughness. By understanding the above α-dependent swelling behaviours and mechanical properties, we calculated the χ_{eff} for hydrogels at different α values using the synthesis–swelling model (Supplementary equation (7)). The χ_{eff} of PAA hydrogels reduced from 0.44 to −1.33 by increasing α from 0 to 0.6 and then stayed relatively stable at $\alpha > 0.6$. The α-dependent χ_{eff} was then fitted by a nonlinear curve (Fig. 2c). In addition, we evaluated the elastic network-chain molecular weights (M_c) based on the measured compressive moduli after swelling equilibrium (Supplementary equation (23)). It was found that the expected ideal network chain

length between crosslinks (N_c) linearly correlated with the measured M_c for the PAA hydrogels (Fig. 2d).

Based on the experimental results and numerical analyses, we established an experimentally validated synthesis–swelling model to describe the swelling behaviours and mechanical properties of the PAA-based AEH system. These model parameters were obtained from the hydrogels consisting of 1.0% PEGDA with various α values, and thus, the experimental swelling results were well captured by the model-predicted results (Fig. 2e). The modelled swelling ratios were also close to the experiment results of hydrogels produced with other PEGDA contents (0.1% and 5.0%), suggesting suitable accuracy of the numerical model. Using such a model, we further plotted the colour contour of the equilibrium swelling ratio as functions of crosslinking content and α, to guide the design of AEHs with controlled swelling (Fig. 2f). As expected, increasing the α and reducing the crosslinker content could enhance equilibrium swelling. The hydrogels with low crosslinking densities, such as 0.1%, enabled a widely tunable swelling ratio from 2 to 50 by altering the α from 0 to 0.7. Similarly, numerical modelling of hydrogel moduli after swelling was performed using the synthesis–swelling theory. The model-predicted results were consistent with the experimental results for hydrogels of various crosslinker concentrations at different ionization states (Fig. 2g). Using the modelling results, we plotted the colour contour of shear moduli as functions of crosslinker content and α (Fig. 2h). The results revealed that the modulus was primarily determined by the crosslinker content and less sensitive to α. It should be noted that AEHs with a low crosslinker content at 0.1% possessed shear moduli of 3–7 kPa (or Young's moduli of 9–21 kPa) that fall in the range of some very soft tissues (for example, liver and lung), while higher crosslinker contents would facilitate higher moduli of the hydrogels to match those of additional tissue types, such as the skin (~100 kPa) (Fig. 2i).

4D printing of AEHs with tunable swelling and mechanics

Built upon the above AEHs, we next illustrated the direct printing of geometry-complex 3D structures with different swelling behaviours and mechanical properties towards self-expansion. We first printed a human nose with tunable swelling by changing M_w (250–3,400 g mol^{-1}) of the 1.0% PEGDA crosslinkers. The hydrogels with crosslinker M_w below 1,000 g mol^{-1} exhibited similar swelling ratios of approximately 10 for AEHs at $\alpha = 0.3$ (Fig. 3a). However, much higher crosslinker M_w (3,400 g mol^{-1}) resulted in large swelling equilibrium ratios (20–30) (Fig. 3b,c). This showed that the entanglements (as physical crosslinks) could outnumber the chemical crosslinks when using low contents of crosslinker or high-M_w crosslinkers, which was confirmed by similar equilibrium swelling ratios for hydrogels using the PEGDA-3400 crosslinker and that without the crosslinker. Moreover, the compressive moduli of hydrogels with PEGDA crosslinkers with increasing M_w of 250–1,000 g mol^{-1} were found to be positively correlated. Nevertheless, the modulus of hydrogels produced with PEGDA-3400 dropped to 18 ± 2.0 kPa, while the opposite trend was seen in the compression strength. It is attributed to the fact that the average chain length between the two adjacent crosslinks ($\bar{M}_c$, Supplementary equation (23)) is reversely related to the stiffness of the hydrogel[33]. Therefore, when the $\bar{M}_c$ in the hydrogel network is higher, the compressive modulus of the hydrogel becomes lower, and vice versa. By contrast, the trend of the hydrogel compressive strength shows the reverse. For practical applications, it should be noted that both the hydrogel's compressive modulus and strength need to be taken into consideration and co-optimized.

The swelling behaviours of 3D-printed constructs could also be facilely adjusted by altering the crosslinker (PEGDA-1000) content. As revealed in Fig. 3d, the printed cone was able to swell isotopically many times its original size while maintaining the high-fidelity mesh structure. Consistent with previous results, a lower crosslinker content would tremendously increase the swelling ratio and reduce the stiffness (Fig. 3e,f and Supplementary Figs. 5 and 6). We further realized multi-material printing of constructs with anisotropic shape-shifting using hydrogels with different PEGDA contents as building blocks. In Fig. 3g, two-dimensional (2D)-to-3D shape-shifting was illustrated by printing a planer film with patterned concentric circles with reducing PEGDA concentrations from the exterior to the interior (that is, regions I, II and III with 0.1%, 2.0% and 10.0% crosslinker, respectively). Upon swelling in normal saline, the printed 2D film transformed into a 3D hemispherical shape after 24 h (Fig. 3h). The anisotropic swelling was quantified by the different changes in dimensions for the inner circular diameter, the outer annular diameter and the height before and after swelling (Fig. 3h,i). It was observed that the expansion of the inner part was restricted by the outer portion, where the deformation mismatch drove the reconfiguration of the 2D film to a 3D dome.

Similarly, the expansion degree mismatch of different hydrogels can be used to trigger 3D-to-3D shape-morphing. As shown in Fig. 3j, a stacked structure was designed to customize the shape-changing from a cylinder to a truncated cone, where the concentrations of PEGDA from regions I to IV were 10.0%, 5.0%, 2.0% and 0.1%, respectively. After soaking the multi-layered cylinder in normal saline, it successfully transformed into a cone shape as a result of the gradient swelling of the layers (Fig. 3k,l and Supplementary Video 3). As a demonstration, we also achieved curling by using the film samples. In Fig. 3m, rectangular films with alternatively distributed hard and soft strips (60° relative to the longitudinal direction) with distinct swelling ratios were designed, where the PEGDA concentrations of stripes I and II with equal width were 10.0% and 0.1%, respectively. The hydrogel film's differential swelling caused the rectangular film to assume bending perpendicular to the direction of the stripes, forming a tubular coil geometry[36] (Fig. 3n and Supplementary Video 4).

Adaptive swelling, mechanical properties and in vitro cytocompatibility of AEH-TEs

Previous clinical outcomes and in vivo experimental reports have suggested that the self-inflating tissue expander should meet at least three requirements: (1) enough swelling capacity to fully expand the prefabricated flap, (2) superior strength to resist skin tension during expansion and (3) suitable stiffness to resist necessary strain and maintain the intact structure under compression from the covering skin tissue, in addition to the sustained expansion scheme unique to our AEHs. Regarding the first requirement, our AEHs enabled large swelling ratios of 10–30, which are much higher than those of previously reported PEGDA-based self-expanding tissue expanders typically at 8–9 (ref. 23). Although the NVP–MMA-based tissue expanders exhibited decent expansion ratios of up to 22 in saline, their mechanical properties were not satisfactory for practical applications[18,21]; the compressive strengths were reported to be merely ~20 kPa with the failure strains of only ~30%[19], leading to easy fracture or unwanted deformation during expansion. With this in mind, we set the following mechanical performance thresholds for the optimized ink formulation after a comprehensive evaluation of the relevant properties required for tissue expanders: (1) compressive modulus ~100 kPa, (2) compressive strength ~100 kPa and (3) failure strain greater than 55%. Accordingly, the hydrogels consisting of 1.0% PEGDA-1000 crosslinker showing an equilibrium swelling Young's modulus of 92 kPa turned out to be a good candidate for application under the skin (stiffness, ~100 kPa) (Supplementary Fig. 7). The matching mechanical properties can provide satisfactory swelling capacity, stiffness, strength and toughness during deformation, as well as sufficient mechanical resistance to skin retraction force-induced tissue expander collapse[23].

We hypothesized that, in our design, the gradual change of ionization of AEHs in biofluids would consecutively enhance the equilibrium swelling ratio towards favourable prolonged self-expansion behaviours. Thus, we investigated the pH-dependent swelling behaviours of AEHs. We used the ink of 50.0% AA-precursor and 1.0% PEGDA-1000

https://doi.org/10.1038/s41551-026-01681-z

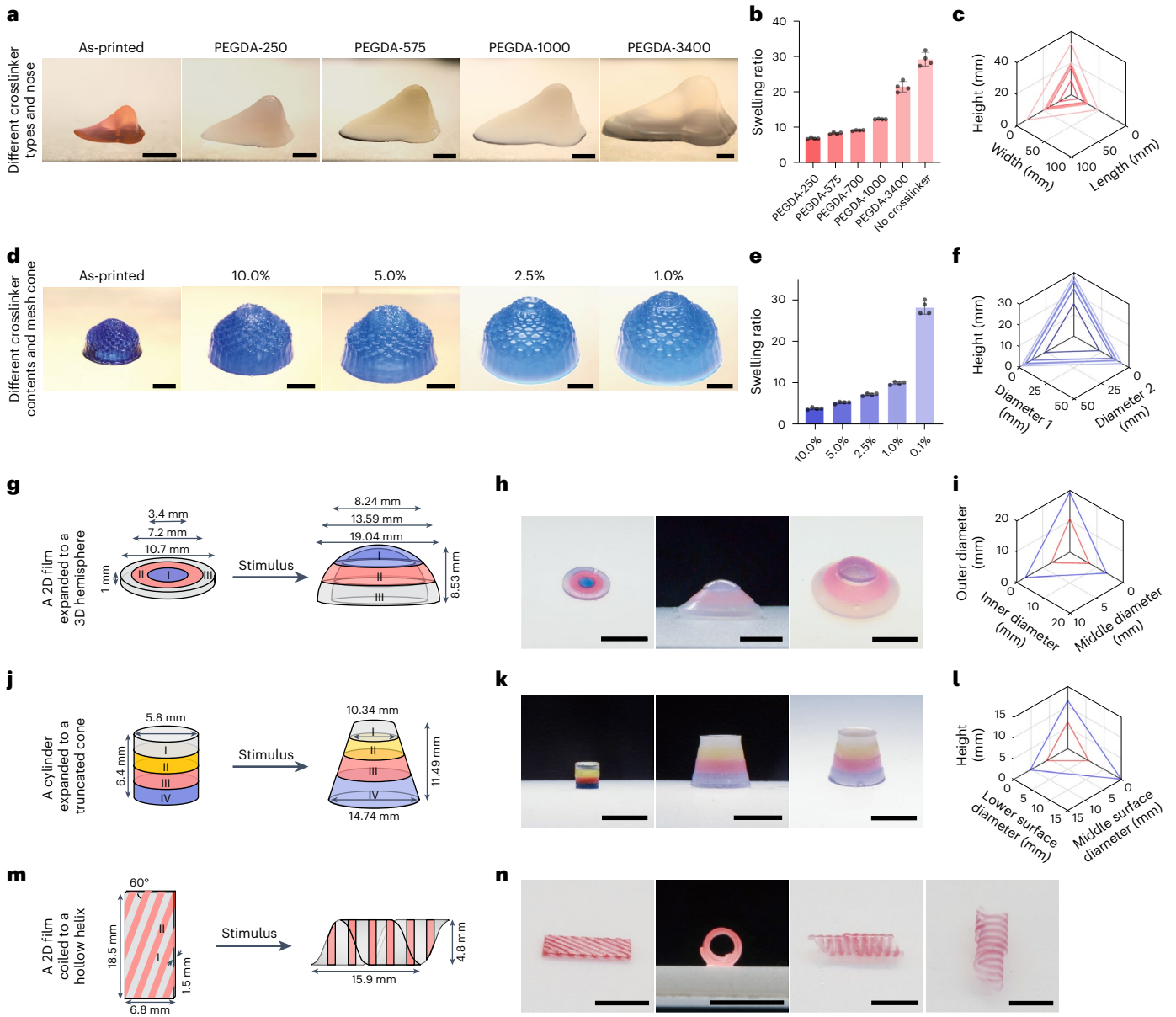

Fig. 3 | 4D printing of assorted AEH-based structures for isotropic and anisotropic expansion. a–**c**, Isotropic swelling behaviour of the printed nose constructs using different PEGDA crosslinker M_w as labelled: photographs (**a**), mass swelling ratios (mean ± s.d., $n = 4$ biological replicates) (**b**) and dimensions of swollen constructs (**c**). **d**–**f**, Isotropic equilibrium swelling behaviours of the printed cone constructs using different contents of PEGDA-1000 crosslinker: photographs (**d**), mass swelling ratios (mean ± s.d., $n = 4$ biological replicates) (**e**) and dimensions after equilibrium swelling (**f**). **g**–**i**, 2D-to-3D shape-shifting of a printed multi-material disk consisting of three concentric rings of different AEHs shifting to a dome shape: scheme and marked dimensions (**g**), photographs before and after shape-shifting (**h**) and diameters of each ring before and after shape-shifting (**i**). Red, the original printed dimension; blue, the dimension after shape-morphing. Regions I, II and III refer to 0.1%, 2.0% and 10.0% crosslinker, respecitvely. **j**–**l**, 3D-to-3D shape-shifting of a printed four-layered cylinder of different AEHs shifting to a cone shape: scheme and marked dimensions (**j**), photographs before and after shape-shifting (**k**) and diameters of each cylinder segment before and after shape-shifting (**l**). Red, the original printed dimension; blue, the dimension after shape-morphing. Regions I, II, III and IV refer to 10.0%, 5.0%, 2.0% and 0.1% crosslinker, respectively. **m**,**n**, 2D-to-3D shape-shifting of a printed multi-material film shifting to a coil: scheme and marked dimensions (**m**) and photographs before and after shape-shifting (**n**). All samples were printed with an identical initial $\alpha = 0.3$ and soaked in normal saline for swelling. Regions I and II refer to 10.0% and 0.1% crosslinker, respectively. Scale bars, 1 cm.

to print ear-shaped constructs. After printing, the ear structures (~0.2 g each) were soaked in pure normal saline (200 ml), reaching an equilibrium swelling ratio of 1.7 with a medium pH of 2.8 in 3 days. Afterwards, we adjusted the medium pH to 4, 5, 6, 7 and 8 using 5 M NaOH solution step-wise to reach the average equilibrium swelling ratios of 4.0, 5.6, 8.0, 10.2 and 12.4, respectively, with a 3 day interval for each swelling duration (Fig. 4a,b). The printed ear model (termed ear-shaped AEH-TE or AEH-e-TE; initial α of 0) with an original size of 17 × 9.5 mm^2 gradually expanded at the stepwise increasing $-OH^-$ and reached an ultimate equilibrium swelling size of 43 × 24 mm^2 in the adequate buffer (initial pH = 8) (Fig. 4a). This environment-adaptive swelling was also observed in AEHs with a higher initial ionization ($\alpha = 0.4$), showing an initial swelling ratio of 9.4 in normal saline (pH = 6.3) and then increased swelling ratio up to ~11 after adjusting the medium pH to 7 by adding NaOH in the swelling buffer (Fig. 4c).

It was, however, noted that the residual AA monomers within the crosslinked hydrogels could result in an acidic environment in vivo, leading to noninfectious inflammation and even tissue necrosis.

We thus also tested the swelling behaviours of purified AEHs. The purification process by dialysis in normal saline followed by shrinking in 30.0% NaCl could not only purify these hydrogels but also recover the original sizes of the AEHs without altering the initial ionization degrees. Therefore, environment-dependent adaptive swelling behaviours were observed in the purified and shrunken AEH-e-TEs (Fig. 4d) to almost the same level as the pristine AEH-e-TEs without any treatment (Fig. 4b). Considering the good potential of biocompatibility and reduced inflammation risk under a less acidic microenvironment, we selected the AEHs with initial α of 0 and 0.4 for in-depth in vitro and in vivo assessments. As an illustration, the printed ear construct (α of 0.4) exhibited a swelling ratio of 14.2 during dialysis and was then shrunken to nearly the original size in 30.0% NaCl (end swelling ratio of 1.2) (Fig. 4e). The same device could reswell back to a ratio of 14.1 in normal saline (Fig. 4f).

For all the above experiments, a 0.9% NaCl solution (pH ~7.4) was predominantly used as the swelling buffer, where it was confirmed that the ionization degree affected the final swollen sizes of AEH-TEs. Nevertheless, we hypothesized that AEH-TEs with a low initial ionization degree could achieve a higher ionization degree in buffers containing more abundant electrolytes that better mimic the body fluids. This assumption was indeed validated by the greater swelling ratio of AEH-TEs ($\alpha = 0$) in Dulbecco's phosphate-buffered saline (DPBS; Fig. 4g and Supplementary Fig. 8). To mimic the limited space of the in vivo subcutaneous tissues and the metabolism of body fluids, we further established an in vitro fluidic system to enable AEH-TEs to swell in dynamically flowing DPBS (Supplementary Fig. 9 and Supplementary Video 5). AEH-TEs (with α of 0 and 0.4) swelled gradually and reached their target sizes eventually (Fig. 4h–j and Supplementary Fig. 10).

To evaluate the feasibility of using AEH-TEs as in vivo implants, we first conducted in vitro cellular assays. The viabilities, proliferation and morphologies of both human foreskin fibroblasts-1 (HFF-1) and human mammary epithelial cells (HMECs) were assessed via live/dead and F-actin staining[37,38]. To investigate the impact of hydrogel swelling on cells, AEH-TE films (α of 0 and 0.4) were individually placed into transwell inserts. The cells were then seeded onto 6-well plates containing these transwell inserts; after 7 days of culture, the hydrogel films were fully swollen (Supplementary Fig. 11). On both day 1 and day 7, no notable differences were observed in either live/dead or F-actin staining results (Supplementary Figs. 12 and 13). The 3-(4,5-dimethylthiazol-2-yl)-2,5-diphenyltetrazolium bromide (MTT) assays were additionally performed to validate these findings. The relative metabolic activities of the cells cultured in AEH-TE-treated media were comparable to those in regular media (Supplementary Fig. 14).

In addition, the as-printed and purified AEHs showed comparable and favourable mechanical properties (Fig. 4k–m). The purified AEHs showed a fracture strain of 500% and a tensile strength of 400 kPa, similar to those of the as-printed samples (Fig. 4k,l). After self-expansion (swelling ratio at ~15), the purified AEHs exhibited a compressive strength of over 200 kPa and a break strain of over 60%, which still met our intended metrics and were comparable with those of the as-printed devices after expansion (Fig. 4m). Accordingly, we rationed that these 4D-printed AEH-e-TEs with environmentally adaptive large swelling and good mechanical properties would likely reveal satisfactory performances in vivo.

4D-printed AEH-TEs for external ear and breast reconstruction surgery and comparisons with current clinical devices

Microtia is a congenital malformation that manifests mainly as the partial or complete absence of external auricle, with an incidence of 0.83 to 17.4 per 10,000 births worldwide[39–41], meaning that millions of patients are suffering from both physical and psychological pains generated from microtia. Currently, ear reconstruction using autologous costal cartilage grafting is the gold standard for the treatment of microtia[42]. Many patients, especially in the Asian population, have a thicker skin, a weaker cartilage and a limited skin volume, increasing the risk of skin necrosis and deformation of the ear scaffold after implantation[17]. The emergence of ear reconstruction using the tissue-expansion technique has widely benefited these patients by solving the deficiency of the skin tissue. Such a technique has become one of the most important approaches to treat microtia[17], where moulded rectangular and other simple-shaped tissue expanders were previously used in skin flap pre-fabrication before ear reconstruction surgery[16,43,44]. To test the potential clinical applications of specific-shaped self-expanding tissue expanders, we first 4D-printed AEH-e-TEs as a proof-of-concept demonstration targeting the microtia patient population (Fig. 5a). It should be noted that the expansion ratio of ~15 attainable with the selected AEH with an initial α of 0.4 is more than sufficient for this intended application scenario, although higher expansion ratios are possible with AEHs of other ionization degrees.

Of clinical importance, the temporary implants that will be explanted after a certain time should be easily removed, have good biocompatibility that does not introduce toxic by-products during the in vivo period, be non-toxic or have low toxicity, and at least leave no long-term side effects to the human body. The as-printed AEH-e-TEs (without purification) were implanted into a rabbit model. Necrosis was unsurprisingly seen in most portions of the covering skin tissue on day 2 of implantation owing to the toxic residual monomers of AA (Supplementary Fig. 15). After treatment with dialysis (in normal saline for 3 days) and shrinkage (in 30.0% NaCl for 3 days), the residual monomers were completely removed from the AEH-e-TEs, and suitable biocompatibility could be obtained. The chemical compositions of the AEH polymer matrices were confirmed by Fourier-transform infrared (FTIR) spectra with major band assignments (Supplementary Table 4 and Supplementary Fig. 16). The $\alpha = 0$ AEH was a typical PAA hydrogel featuring a carboxylic acid group ($\upsilon_{C=O} = 1{,}700\ cm^{-1}$), and the $\alpha = 0.4$ AEH was a poly(AA-co-NaAA) copolymer exhibiting partial ionization ($\upsilon_{COO^-,asym} = 1{,}541\ cm^{-1}$). FTIR spectra also confirmed negligible residual AA monomers for as-prepared AEHs with different α. The elemental differences of AEHs were studied by energy-dispersive X-ray spectroscopy

Fig. 4 | In vitro swelling behaviours and mechanical properties of 4D-printed AEH-e-TEs. a, Photographs showing the representative gradient equilibrium swelling of a dialysed/re-shrunken printed AEH-e-TE (with initial $\alpha = 0$) before and after sequentially adjusting the pH value from 4 to 8. Scale bar, 2 cm. **b**,**c**, Gradient equilibrium swelling of as-printed AEH-e-TEs with two different initial degrees of ionization: $\alpha = 0$ (mean ± s.d., $n = 3$ biological replicates) (**b**) and $\alpha = 0.4$ (mean ± s.d., $n = 3$ biological replicates) (**c**). The as-printed ear constructs were immersed in normal saline, and the pH value was gradually adjusted to neutral in multiple steps to reach the equilibrium swelling. **d**, Gradient equilibrium swelling of the dialysed printed AEH-e-TEs with an initial $\alpha = 0$. The as-printed AEH-e-TEs were dialysed in normal saline and were re-shrunken in 30.0% NaCl solution, followed by sequentially adjusting the medium pH values for a two-step swelling (mean ± s.d., $n = 3$ biological replicates). **e**,**f**, Gradient equilibrium swelling of the dialysed AEH-e-TEs with an initial $\alpha = 0.4$ during the process of dialysis, re-shrinking and re-swelling: equilibrium swelling ratios (mean ± s.d., $n = 3$ biological replicates) (**e**) and photographs (**f**). Scale bar, 2 cm. **g**, Expansion of AEH-TEs ($\alpha = 0$ and 0.4) in different buffers (mean ± s.d., $n = 4$ biological replicates); two-sided unpaired t-test. **h**–**j**, Expansion of AEH-TEs in the in vitro fluidic system: photographs of an $\alpha = 0.4$ AEH-TEs in the in vitro fluidic system at different time points (mean ± s.d., $n = 4$ biological replicates) (**h**), photographs of changes of an $\alpha = 0.4$ AEH-TEs extracted from the in vitro fluidic system at different time points (**i**) and swelling curves of AEH-TEs in the in vitro fluidic system (mean ± s.d., $n = 3$ biological replicates) (**j**). Scale bars, 2 cm. **k**–**m**, Mechanical properties of original and purified AEHs by dialysis and re-shrinking treatments: photographs showing the high-strain stretching of AEH samples (**k**), stress–strain curves (**l**) and compressive stress–strain curves (**m**). Scale bar, 1 cm. Equilibrium swelling was reached in the 3 day soaking process in each step.

https://doi.org/10.1038/s41551-026-01681-z

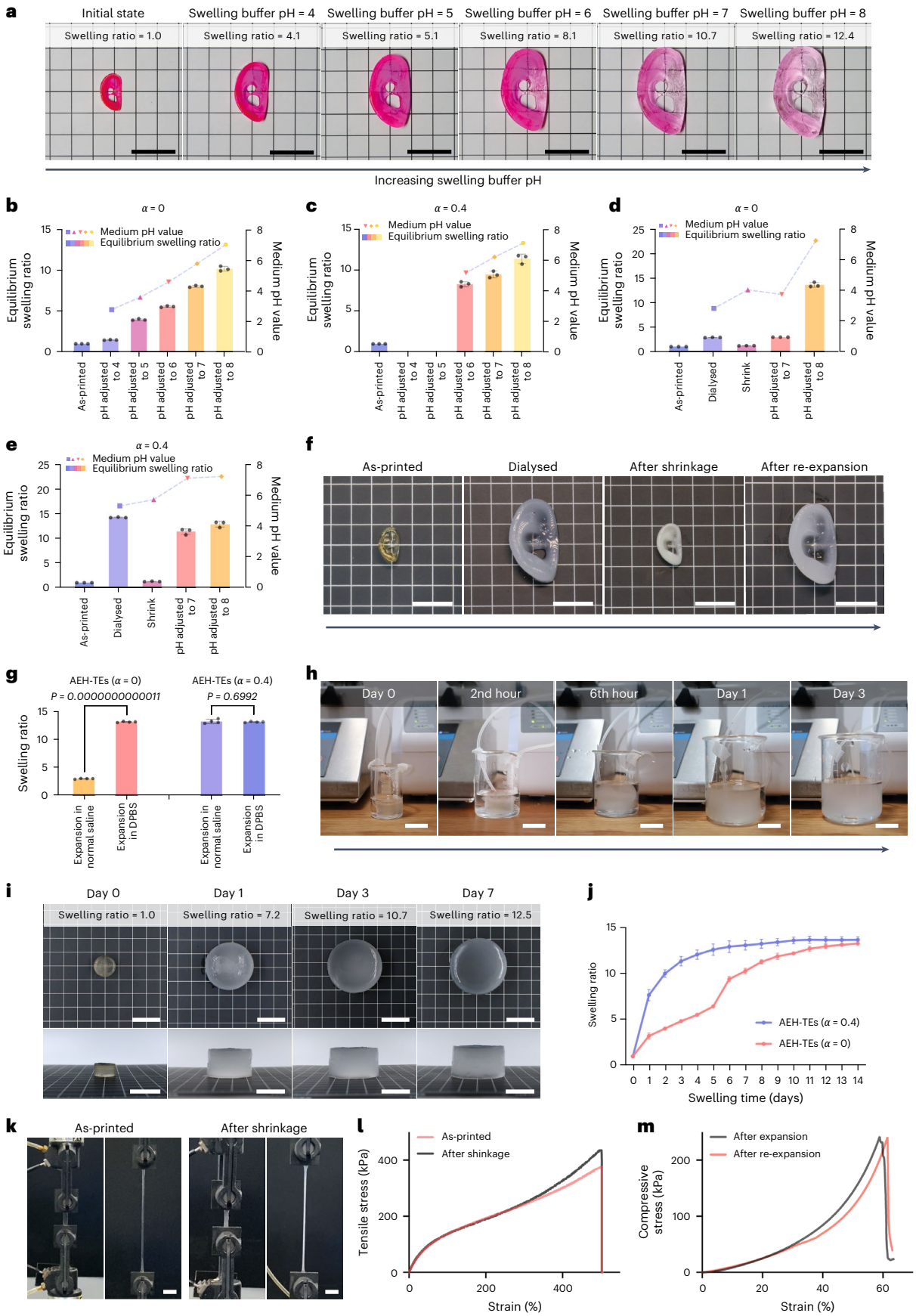

(EDS) (Supplementary Table 5 and Supplementary Figs. 17 and 18). The $\alpha = 0$ AEH revealed negligible sodium element, whereas the sodium content increased to 12.47% in the $\alpha = 0.4$ AEH, further boosted to 17.84% after dialysis owing to the trapped sodium chloride. The low concentrations of the AA monomer residuals in the 3D-printed AEH-TEs could be almost entirely removed by dialysis treatment in saline (Supplementary Fig. 19), enabling suitable in vivo biocompatibility.

Another key benefit of dialysis treatment was the reduction of tissue adhesion, facilitating minimally invasive operations. We performed 180° peel tests for both as-printed and dialysed hydrogel films. The as-printed hydrogel film presented strong adhesion, and it took an average load of 0.47 N (adhesion energy of 47 J m^{-2}) to peel apart the two pieces of attached rabbit skins (Supplementary Fig. 20). The strong adhesion of as-printed AEH-e-TEs to the body was also confirmed in animal experiments; by contrast, after dialysis/re-shrinking treatments, the AEH-e-TEs showed negligible adhesion (Supplementary Video 6).

Next, we conducted full in vivo tests using the purified AEH-e-TEs by implanting them under the skins of rabbit's backs. We captured photographs of the implanted region through a digital camera and 3D images using computed tomography (CT) (Fig. 5b). The ultimate objective of the tissue-expansion technique is to prefabricate skin flaps and augment surface areas of the skins, thereby achieving larger skin tissues with robust blood supplies. Clinically, the critical metrics for evaluations are whether the skin size has been increased and whether adequate blood circulations have been effectively established. The area of the covering skin above the AEH-e-TE was calculated from the reconstructed volumetric data, suggesting an area expansion ratio of ~200% after absorption of body fluid in the first 3 days, which was subsequently maintained stable in the following 10 days until 2 weeks, the time of explantation (Fig. 5b and Supplementary Fig. 21). The implant showed good tissue apposition under the subcutaneous layer, with a clear contour (Fig. 5b(iv)). In an effective expansion process, the dermis becomes thinner over time with an increase in the surface area of the skin tissue[45]. In our experiments, we also noticed the decreasing dermis thickness of the experimental groups from 2,633.31 µm to 1,134.55 µm (more than 2 times) at 2 weeks of AEH-e-TE implantation (Fig. 5c).

Cell proliferation and neovascularization correlated with tissue regeneration are typical changes in expanded tissues[10,11]. In the gross view of the expanded area on day 14, accompanied by the increase in the skin area, the elevation in vascularity of the expanded skin was visually observed (Fig. 5b(ii)). This observation forms the typical indication of the flap-delay phenomenon, which helps the surgeon to obtain larger or longer flaps for reconstruction[45]. Angiogenesis of the expanded skin was confirmed by histological staining with trichome and immunofluorescent staining of CD34 (Fig. 5d,e). The data suggested that the printed AEH-e-TEs vastly increased the vascularity of the skin tissue, reportedly to be driven by the increasing amount of vascular endothelial growth factors in the expanded tissue, resulting in the proliferation of blood vessels[15]. The proliferating cell nuclear antigen (PCNA) is a cell cycle-regulated nuclear protein, and its synthesis rate correlates well with the proliferative status of the cell[46]. PCNA was further stained to detect proliferating cells in the basal layer (the origin of the epithelial layer). In the experimental group, PCNA was found to be strongly positive, which showed that cells in the expanded skin flap proliferated rapidly (Fig. 5e and Supplementary Fig. 22). This is a response to stress from the expansion of AEH-e-TEs, which can open the stretch-induced ion channels, produce secondary messengers and eventually lead to cell proliferation[45]. These fundamental mechanisms, however, are out of scope for the current work to explore.

We then analysed the in vivo biocompatibility of AEH-e-TEs. As a temporarily exogenous implant, a tissue expander oftentimes inevitably induces local inflammation, termed the foreign body responses. These responses usually contribute to forming a capsule of dense fibrous tissue surrounding the implant within a time frame of several days[47]. To evaluate the overall biocompatibility, we assessed both acute (less than 24 h) and subacute (24 h to 30 days) systemic toxicity upon implantation of the AEH-e-TEs by routine blood tests and detection of inflammatory biomarkers from blood samples of rabbits at predefined time points, considering the recommendation by the US Food and Drug Administration (FDA-2021-N-0334). White blood cells, granulocytes, lymphocytes and monocytes are the main signs of systemic inflammation. The blood tests indicated that the counts of these cells varied almost within the normal reference ranges for rabbit blood samples both before and after the implantation (Fig. 5f)[48]. Next, we investigated the inflammation at a more microcosmic level using inflammation markers. C-reactive protein is a classic sensitive index of graft rejection and chronic low-grade inflammation[49]. C-reactive protein is considered to be associated with abnormalities following synthetic polymer implantation[50]. In addition, serum amyloid A is the major acute-phase protein that acts as a biomarker of inflammation[51]. Pro-inflammatory cytokines interleukin 1-β (IL-1β) is also involved in the early innate immune responses[47,52]. All these three biomarkers showed negligible differences between pre-operation and post-operation from day 1 to day 14 (Fig. 5g). The data suggested that no notable systemic inflammation was observed upon AEH-e-TE implantation, revealing good biocompatibility up to at least 14 days evaluated.

In recent decades, self-expanding soft tissue expanders have been used in ophthalmology and stomatology and, occasionally, in reconstructive and plastic surgeries, such as the Osmed osmotic tissue expander, one of the more widely used self-inflating soft tissue expanders in clinical settings[22,53]. However, issues with uncontrolled rapid expansion and relatively high complication rates have prevented these devices from becoming standard clinical tools, and in fact, they are rarely used anymore today[20,54–56]. To highlight the advantages of our devices over other self-expanding tissue expanders, we first synthesized a hydrogel with a swelling ratio of ~10 in normal saline for comparison, using the primary material system (NVP–MMA) of the Osmed osmotic tissue expander[22,53].

Cylindrical AEH-TEs (with $\alpha = 0$ and $\alpha = 0.4$) and NVP–MMA hydrogel discs of the same size were fabricated. Although sufficiently

Fig. 5 | In vivo effectiveness and safety validations of 4D-printed AEH-TEs. **a**, Scheme showing the procedures, including DLP printing of the personalizable AEH-e-TE for implantation and expansion in vivo. **b**, Photographs and CT scanning images of a subcutaneously implanted AEH-e-TE at selected time points ($n = 3$ biological replicates). (i) Implanted device at day 0. (ii) Top view of implanted device at day 14. (iii) Lateral view of impanted device at day 14. (iv) CT scanning image of implanted device at day 14. Scale bars, 1 cm. **c**, Calculated skin areas from CT-scanning results for the experimental group on day 0 and day 14 of AEH-e-TE implantation (mean ± s.d., $n = 3$ biological replicates); two-sided unpaired t-test. **d**, Masson's trichrome staining of unexpanded skin tissue (i) and expanded skin tissue (ii, iii) ($n = 3$ biological replicates) and dermal thickness comparison of unexpanded and expanded skin tissues (mean ± s.d., $n = 3$ biological replicates); two-sided unpaired t-test (iv). Black arrows indicate neovessels of the expanded flap. Scale bars, 500 µm. **e**, Immunofluorescence staining for CD34 and PCNA of unexpanded and expanded skin tissues ($n = 3$ biological replicates). White arrows indicate neovessels of the expanded flap. Scale bars, 100 µm. **f**, Routine blood tests for experimental rabbits' venous blood at different time points for white blood cells (WBC), granulocytes (GRA), lymphocytes (LYM) and monocytes (MON). Grey backgrounds indicate the ranges of normal values. Three coloured lines represent samples collected from three different rabbits. **g**, Quantifications of key soluble biomarkers of inflammation for venous blood collected from rabbits in the experimental group at different time points of AEH-e-TE implantation: C-reactive protein (CPR), serum amyloid A (SAA) and IL-1β (mean ± s.d., $n = 3$ biological replicates); ordinary one-way ANOVA. Schematic in **a** created in BioRender; Wang, D. https://BioRender.com/b2meplp (2026).

https://doi.org/10.1038/s41551-026-01681-z

swollen NVP–MMA hydrogel discs could reach a size comparable to our AEH-TEs (Supplementary Fig. 23), they were substantially less robust (Supplementary Fig. 24). Cylindrical AEH-TEs and NVP–MMA hydrogel discs were subsequently implanted beneath the skin at the hypochondrium of rabbits and explanted at day 7 (Fig. 6a and Supplementary Fig. 25a). All AEH-TEs gradually expanded over the following week. Notably, the AEH-TEs with an initial α of 0.4 maintained their cylindrical shape throughout, while those with $\alpha = 0$ experienced minor edge damage towards the end of expansion. However, devices in the NVP–MMA group began to break already between days 2 and 4, eventually losing their entire shape as a result of the skin tension and the external forces caused by the rabbits' movement and self-inflicted

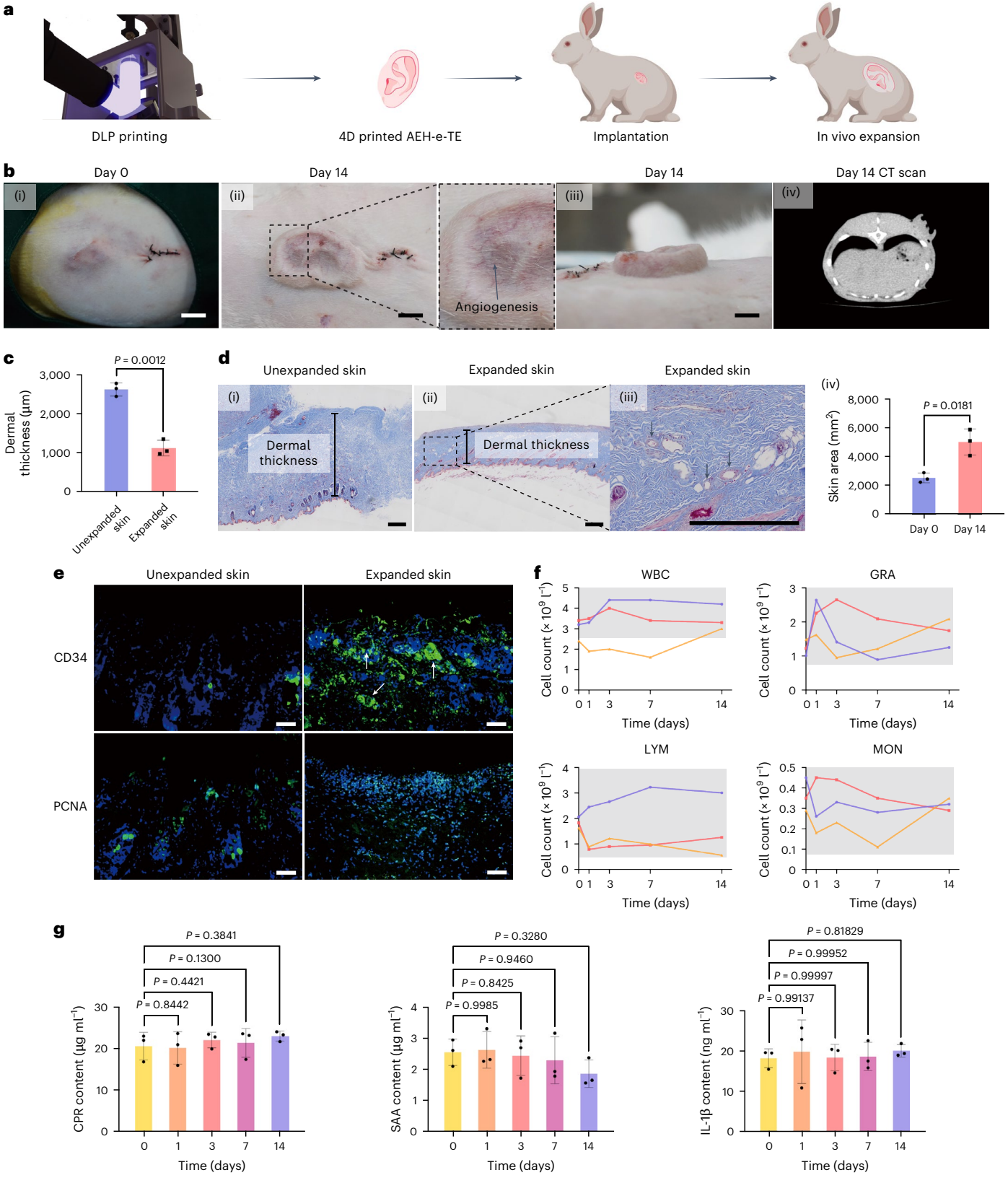

https://doi.org/10.1038/s41551-026-01681-z

injuries. Compared to expanding the mucosal tissue in ophthalmologic and stomatologic surgeries, expanding skin tissue in reconstructive operations withstands substantially greater forces generated from skin tension. As shown in Fig. 6b and Supplementary Figs. 25b–d, the AEH-TEs with $\alpha = 0$ exhibited the slowest expansion rate among the three groups but adaptively expanded to more than 10 times their original size, verifying the environment-dependent swelling behaviour of AEHs (Fig. 4a,b).

Body fluids in vivo are in a dynamic equilibrium state of continuous circulation. Compared with conventional hydrogel swelling governed purely by water diffusion, the swelling of the AEHs is controlled by coupled water and electrolyte diffusion. In our AEH, the water–polymer interactions dynamically change with hydrogel ionization, leading to environment-adaptive equilibrium swelling ratios. In body fluid with a relative stable and neutral pH, the AEHs would rapidly swell by absorbing the water. Meanwhile, the diffused electrolytes will slowly neutralize the AEHs and modify the degree of ionization stepwise, exhibiting electrolyte-controlled prolonged swelling in a clinical setting. As body fluids are continuously replenished, electrolytes are also steadily supplied. Therefore, as long as body fluids are consistently available, even in a relatively fluid-poor environment such as the subcutaneous body surface, the driving force for the continuous swelling of AEH-TEs, irrespective of their sizes, will persist until final swelling equilibrium is reached, as well illustrated in both in vitro and in vivo experiments.

In addition, while a fluid-poor or slow-fluid-supply condition may delay the swelling rate of large-sized AEH-TEs, this is in fact an important advantage of our devices, enabling slow, stable and substantial swelling and achieving gradual and sufficient tissue expansion and flap prefabrication. If rapid and substantial expansion occurs in a short period, the flap may face risks of ischaemia, hypoxia or even necrosis[57]. AEH-TEs with a low initial α require a longer time to reach swelling equilibrium than those with a high initial α, and this phenomenon has been verified through both in vitro (Fig. 4h,i and Supplementary Fig. 10) and in vivo (Fig. 6a and Supplementary Fig. 25) experiments. This is because environment-adaptive AEH-TEs with different initial α need varying amounts of electrolytes and time to undergo further ionization. Different expansion rates cater to diverse clinical needs, such as intraoperative, acute and chronic tissue expansion[58,59]. In future studies, we will conduct in-depth exploration of the relevant scientific issues.

To further assess the translational potential of AEH-TEs and their unique superiority over current clinical devices, we simulated the ear reconstruction surgery using AHE-e-TEs and the kidney-shaped silicone tissue expanders, a clinical standard used today (Fig. 6c,d and Supplementary Fig. 25). We conducted multi-stage procedures closely replicating the real surgery (Supplementary Videos 6–8). In this comparative experiment, we printed larger AEH-e-TEs capable of expanding to the size of a typical human auricle (~5.5–6.5 cm in length, ~2.8–3.3 cm in width and ~1.6–1.8 cm in auriculocranial height)[60]. As a control, we implanted 50 ml kidney-shaped silicone expanders—the most commonly used size in ear reconstruction surgery[61]—into rabbits, followed by daily repeated saline injections to induce expansion. During stage I, all devices were implanted at the hypochondrium, simulating the postauricular region (mastoid) to achieve maximum protrusion after expansion under the skin. After 10 days of in vivo expansion, we performed stage II operations. All devices were explanted, and 3D-printed auricle prostheses of the same shape and size as the expanded AEH-e-TEs (and hence the real human ear) were individually placed into the expanded pockets (Supplementary Figs. 26 and 27 and Supplementary Videos 7 and 8). We adopted 3D-printed prostheses instead of autologous cartilage frameworks otherwise used clinically to (1) ensure uniformity across experimental groups and (2) simulate the possible future use of 3D-(bio)printed tissue-engineered auricle implants[62–64].

Using AEH-e-TEs (with $\alpha = 0$ and $\alpha = 0.4$), we achieved tightly controlled and stable in vivo expansion in stage I procedures. These implants expanded to the desired size without observable displacements, maintaining their 3D auricle shape throughout the entire period (stage I in Fig. 6c and Supplementary Fig. 26-I). Equally importantly, during stage II surgery, we could conveniently remove the expanded devices (stage II(i) in Fig. 6c and Supplementary Fig. 26-II) and implant the auricle prostheses without complications (Supplementary Videos 7 and 8). Consistent with results obtained with disks, AEH-e-TEs with $\alpha = 0$ were less resilient during explantation and were more prone to damage from accidental impacts, although such a difference was not major. After simple negative-pressure suction after implantation of the protheses, we achieved satisfactory and stable reconstructed ears in both groups (stage II(iii–vi) in Fig. 6c, Supplementary Fig. 26-II and Supplementary Video 9).

By sharp contrast, despite the fact that the kidney-shaped silicone devices required additional procedures, they still yielded much

Fig. 6 | In vivo competitive advantages of AEH-e-TEs over existing and clinical devices and evaluations of AEH-b-TEs for breast-reconstruction surgery. **a**, Photographic records of implantations of cylindrical AEH-TEs ($\alpha = 0.4$) and NVP–MMA tissue expanders beneath the skins of rabbits and explanted devices after 1 week. (i) Devices before implantation. (ii)–(v) Top views of implanted device at days 0, 1, 3 and 7, respectively. (vi) Lateral view of implanted device at day 7. (vii) Lateral view of extracted device at day 7. (viii) Top view of extracted device at day 7. Scale bars, 2 cm. **b**, Volume changes of AEH-TEs and NVP–MMA tissue expanders (mean ± s.d., $n = 3$ biological replicates). **c**, Photographic records of the entire ear reconstruction surgery using an AEH-e-TE ($\alpha = 0.4$). In stage I, the device was implanted subcutaneously. (i) Dialysed AEH-e-TE. (ii)–(vi) The implanted device expanded gradually in vivo. (ii)–(v) Top views of implanted device at days 0, 2, 6 and 10, respectively. (vi) Lateral view of implanted device at day 10. In stage II, the device was extracted, and a 3D-printed auricle prothesis of the same shape and size was implanted. (i) Extracted AEH-e-TE. (ii)–(vi) The 3D-printed auricle prothesis was implanted into the precisely expanded pocket and securely held its position for up to 3 days evaluated. (ii), (iii) and (v) Top views of implanted protheses at days 0, 2 and 3, respectively. (iv) and (vi) Later views of implanted device at days 2 and 3, respectively. Scale bars, 2 cm. **d**, Photographic records of the entire ear reconstruction surgery using a clinical-standard 50 ml kidney-shaped silicone tissue expander. In stage I, the device was implanted subcutaneously. (i) Kidney-shaped silicone tissue expander. (ii)–(vi) The implanted device was injected with normal saline daily and expanded gradually in vivo. (ii)–(v) Top views of implanted device at days 0, 2, 6 and 10, respectively. (vi) Later view of implanted device at day 10. In stage II, the device was extracted, and a 3D-printed auricle prothesis was implanted. (i) Extracted kidney-shaped silicone tissue expander. (ii) The expanded skin tissue after extraction of the device. (iii)–(vi) The 3D-printed auricle prothesis was implanted into the overlarge pocket, shifted freely under the skin and located at different positions within the pocket. In stage III, the trimming surgery was performed to remove redundant expanded skin tissue to achieve the position-stable and appearance-satisfactory auricle. (i) The removed redundant skin tissue. (ii) The redundant skin tissue was marked. (iii) and (iv) The marked skin tissue was removed to allow the expanded skin to better match the implanted 3D-printed auricle prothesis (top and lateral views at day 0, respectively). (v) and (vi) The appearance at 3 days after the removal of marked skin tissue (top and lateral views, respectively). Scale bars, 2 cm. **e**, Comparisons of masses of trashed skin tissues between the AEH-e-TE ($\alpha = 0.4$) group and the kidney-shaped silicone tissue expander group (mean ± s.d., $n = 3$ biological replicates); two-sided unpaired t-test. **f**, Comparisons of surgical operation durations between the AEH-e-TE ($\alpha = 0.4$) group and the kidney-shaped silicone tissue expander group (mean ± s.d., $n = 3$ biological replicates); two-sided unpaired t-test. **g**, Comparisons of total incision lengths between the AEH-e-TE ($\alpha = 0.4$) group and the kidney-shaped silicone tissue expander group (mean ± s.d., $n = 3$ biological replicates); two-sided unpaired t-test. **h**, Expansions of AEH-e-TEs ($\alpha = 0.4$) in the normal condition versus the haematoma model. Scale bars, 1 cm. **i**, In vivo evaluations of AEH-b-TEs with an initial base diameter of 4 cm ($\alpha = 0.4$): (i) dialysed AEH-b-TE; (ii)–(vi) the implanted device expanded gradually in vivo at days 0, 1, 4, 7 and 12, respectively; (vii) extracted AEH-b-TE. Scale bars, 2 cm.

https://doi.org/10.1038/s41551-026-01681-z

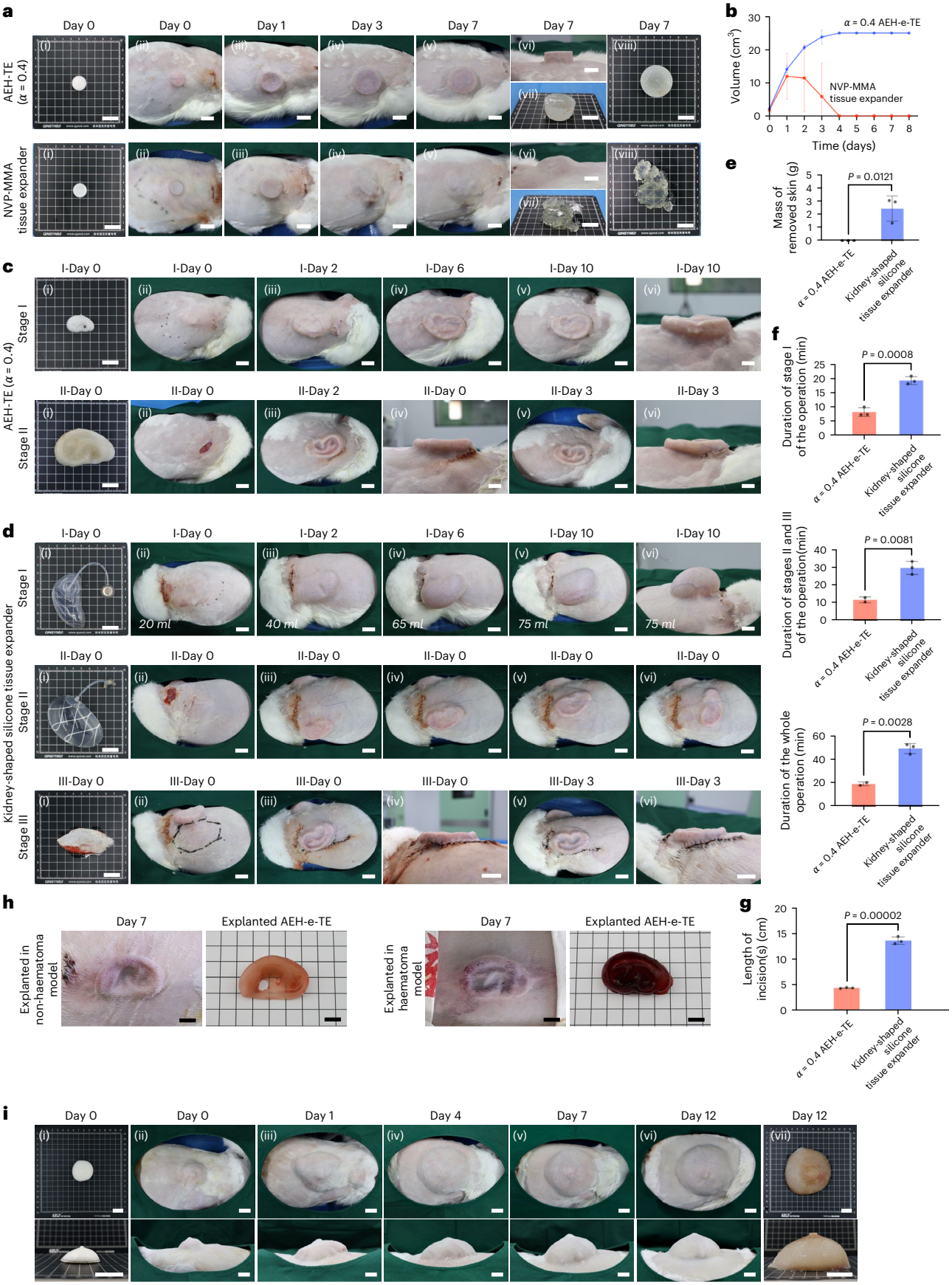

less favourable outcomes (Supplementary Video 10). All silicone tissue expanders migrated from originally implanted locations to varying degrees owing to gravity and the rabbits' movements (stage II(iii)–(vi) in Fig. 6d and Supplementary Fig. 28), which is not uncommon even in human applications[65]. Another complication observed was injection port turnover and connector tube kinking, where the injection port could be dragged or rolled over during expansion (Supplementary Fig. 29), making saline injections extremely challenging. By comparison, our AEH-e-TEs remained securely in place until the end of expansion. In addition, the shape of the expanded skin stretched by the silicone tissue expanders led to excess tissue formation and oversized pockets, resulting in poor positioning and low-definition appearances of the implanted auricle prostheses (stage II(ii)–(vi) in Fig. 6d and Supplementary Video 10). For aesthetic purposes, we had to perform an additional stage III operation (stage III in Fig. 6d) to mark and remove the excess skin, further increasing the injury and recovery time (Fig. 6e and Supplementary Fig. 30). Consequently, not only was there a substantial amount of time wasted on these additional procedures (Fig. 6f), the resulting incisions and scars were also notably larger (Fig. 6g and Supplementary Fig. 31) than the surgeries performed with our AEH-e-TEs.

Surprisingly, the AEH-e-TEs showed a unique yet unexpected advantage in their ability to absorb oozing or bleeding blood, preventing haematoma and using this absorption to aid the swelling process, a capability not seen with other clinical tissue expanders. Haematoma, one of the most common complications after insertion of a tissue expander with the occurrence rate of ~3%, is associated with acute or chronic haemorrhage of the wound after surgery[65]. If not properly managed, it could form severely poor outcomes such as flap necrosis, extraction of implants and reconstruction failure, which would further induce or elevate patient anxiety and discomfort as well as elongated hospitalization periods[45]. Currently, closed suction drains are used after surgery to prevent possible haematoma, but they come with an increased risk of infection[66]. In the initial in vitro validation, the AEH-e-TEs were shown to absorb blood and expand ~12 times, which approached the same swelling degree driven by absorbing normal saline alone (Supplementary Fig. 32). As preventing haematoma during expansion in vivo would make our AEH-e-TEs more attractive to clinicians by minimizing side effects caused by haematoma, we subsequently established a haematoma model in rabbits by severing two visible blood vessels in the expanded pocket and closing the incision without haemostasis. The implanted AEH-e-TEs successfully absorbed the accumulating blood, preventing haematoma formation and expanding to a comparable size as in normal conditions (Fig. 6h and Supplementary Fig. 33).

Finally, to demonstrate the capability of our device for larger-scale tissue reconstruction, we printed breast-shaped AEH-TEs (AEH-b-TEs). Many breast cancer patients still undergo mastectomy, making breast reconstruction an essential component of breast cancer management and care. Tissue-expander-based breast reconstruction is one of the major surgical approaches[67]. Based on general data, the base diameter of an adult female breast (at body height ~160 cm) is ~10–12 cm. Accordingly, we first printed AEH-b-TEs with an initial maximum base diameter of 2 cm (with $\alpha = 0$ and $\alpha = 0.4$), as an alternative to similar-sized AEH-e-TEs for feasibility assessment. After implantation in rabbits, all devices successfully achieved full swelling within several days (Supplementary Fig. 34). We further printed 4 cm AEH-b-TEs, designed to swell to the average human breast size (base diameter ~10 cm), and conducted additional in vivo evaluations (Fig. 6i, Supplementary Fig. 35 and Supplementary Video 11). Consistent with smaller-sized AEH-ETs, the surgical procedure was simple and time efficient. Within seconds of implantation, the AEH-b-TEs automatically anchored in place. In cases of malposition, correction was readily achievable by injecting saline to facilitate repositioning (Supplementary Video 12). Throughout the observation period, the implanted AEH-b-TEs maintained stable placement (Supplementary Video 13). All rabbits exhibited unrestricted mobility and showed no observable signs of pain (Supplementary Video 14). The AEH-b-TEs were fully explanted after 12 days of implantation. Both types of AEH-b-TEs swelled to their target sizes (Supplementary Fig. 36). Following meticulous dissection, the neovascular network was clearly observable in the subcutaneous layer (Supplementary Fig. 37). AEH-b-TEs could achieve sufficient swelling in the rabbits without complications such as tissue necrosis, indicating that the devices have the potential for use towards the reconstruction of large-sized organs in humans.

Outlook

We have demonstrated the design of a negatively charged polyelectrolyte hydrogel photoink system for light-based 4D printing to create personalizable AEH-TEs with prolonged, large expansion ratios and favourable mechanical properties for surface organ and tissue reconstruction surgery (Supplementary Table 6). Our experimental and modelling results revealed the adaptive swelling behaviours and mechanical properties of the polyelectrolyte hydrogels, which could be used to precisely engineer their expansion profiles. Based on the experimentally validated synthesis–swelling model, we rationally designed biocompatible tissue expanders with controlled equilibrium swelling ratios (up to 30 times), tunable stiffness, and high toughness suitable as in vivo implants. The promise for such tissue expanders in translational applications was illustrated by in vivo assessments using 4D-printed AEH-e-TEs for implantation into a rabbit model. AEH-e-TEs effectively prefabricated the local skin flap showing negligible immuno-inflammatory responses while also benefiting the avoidance of possible subcutaneous haematoma after implant insertion. Compared to the current clinical-standard silicone tissue expanders relying on repeated saline injections, our AEH-e-TEs achieved markedly reduced procedural complexity and complications, as well as markedly enhanced surgical outcomes. Similar observations were obtained with AEH-b-TEs for large-tissue reconstruction. Although the in vivo physiological microenvironments around the implanted tissue expanders were hard to control precisely and thus not measured, the prolonged and large swelling was readily observed because of the gradual modification of the local pH level by the steady diffusion of biofluids. In the future, hydrogel tissue expanders with more actively controlled expansion profiles can be further developed to maximize their clinical relevancy. In the future development, silicone cover or other approaches would be adopted to further ensure the integrity of our device in vivo, especially for the AEH-TEs of $\alpha = 0$ with the lowest expansion rate and slightly weaker mechanical strength during expansion under the skin. Nevertheless, the general synthesis–swelling model might provide a strategy to guide the rational design of environmentally adaptive hydrogel devices and, when combined with the 4D printing technique, collectively advance the next generation of tissue expanders for tissue repair and regeneration.

Methods

Preparations of photoinks and NVP–MMA hydrogel precursors

NaOH (Sigma-Aldrich) and AA (Sigma-Aldrich) were dissolved in deionized water at a molar ratio of 0.2:1 to 1.2:1, separately, to prepare the stock solutions. Then, the NaOH solution and the AA solution were mixed by magnetic stirring for 2 h in the dark at room temperature to obtain ionized AANa solutions with a molar ratio of 0.1:1 to 0.6:1 of NaOH to AA. After the addition of TPO powder (Sigma-Aldrich), the AANa solution was stored at 4 °C in the dark.

The AANa-PEGDA (or AA-PEGDA) inks were prepared by adding a certain amount of PEGDA with M_w = 250, 575 or 700 (Sigma-Aldrich) or PEGDA with M_w = 1,000 or 3,400 (Alfa Aesar) to AA (or AANa) solutions in the dark and stirring at room temperature by magnetic stirring for 1 h. To investigate the swelling and mechanical properties of AEH-TEs

with different formulations, we varied one component while keeping the others constant.

To prepare NVP–MMA hydrogel precursors, we incorporated 0.2% of allyl glycidyl ether (Sigma-Aldrich) as a crosslinking agent, along with 0.2% of azobisisobutyronitrile (Sigma-Aldrich) as an initiator. NVP (Sigma-Aldrich) and MMA (Sigma-Aldrich) were added into the mixture at selected weight ratio at room temperature by magnetic stirring for 1 h. Hydrogel-precursor compositions of 12:1, 10:1, 9:1 and 6:1 NVP/MMA were synthesized.

Synthesis of hydrogels

Cylinder-shaped hydrogel samples were fabricated by photocuring the cast hydrogel precursors in polydimethylsiloxane (PDMS, Dow Corning) moulds. To do this, we first cut cylinder-shape acrylic discs (D = 8 mm, H = 2.5 mm; D = 18 mm, H = 10 mm) by laser cutter. The obtained discs were placed in a petri dish, and the liquid PDMS resin was cast on the top for curing in an oven at 80 °C for 3–5 h. The acrylic discs were then removed to obtain the PDMS moulds.

The AANa-PEGDA hydrogel precursors of various compositions were poured into the PDMS moulds and exposed to 405 nm UV light (OmniCure S2000, Excelitas Technologies) for 30–60 s to allow full crosslinking. In some cases, intermittent UV exposure (alternating on and off for several times) was used to avoid violent reactions for some hydrogel monomers. After curing, the cylinder hydrogel samples were quickly demoulded for further characterizations before dehydration.

To fabricate NVP–MMA hydrogels, the mixed solution was poured into a beaker and subjected to degassing using a vacuum pump for 10 to 15 min to ensure the complete removal of bubbles from the solution. After degassing, the solution was carefully transferred to PMDS moulds and placed in a vacuum drying oven. The temperature was gradually elevated from the ambient laboratory temperature of 5 to 60 °C, with close monitoring throughout the heating process to ensure no further bubble formation. Finally, the mixture was allowed to react at 60 °C for 24 h to form the hydrogel discs. All hydrogel compositions were immersed in normal saline to test their swelling ability. Finally, 10:1 NVP–MMA hydrogels with the swelling ratio of ~12 was selected to be used in the following animal experiments.

FTIR characterization of AEHs

The chemical compositions of AEHs were measured on an FTIR spectrometer (Nicolet6700 FT-IR spectrometer, Thermo Fisher Scientific) in a transmission mode using the potassium bromide (KBr) pellet samples. The AEH samples were dehydrated by freeze-drying and grounded into fine powders before analyses. The powder was homogeneously mixed with dry KBr and then loaded into a stainless-steel pellet die to form a transparent disc under a hydraulic press. The FTIR spectra were recorded by averaging 32 scans of the signal at a resolution of 4 cm^{-1} from 400 to 4,000 cm^{-1}. A background spectrum of a blank KBr pellet was collected under identical conditions and subtracted automatically from the sample spectra.

Scanning electron microscopy characterizations of AEHs

Scanning electron microscopy (SEM) was used for microstructural and elemental analyses. The AEH film samples were dehydrated by freeze-drying and cryo-fractured in liquid nitrogen. The crack surfaces were coated with ~9 nm platinum on an ion sputter-coater (GVC-2000, GVC). The samples were observed on a field-emission SEM (Tescan CLARA) under high vacuum at an acceleration voltage of 10 kV and working distance of 8–10 mm. Secondary electron imaging was used to visualize the surface morphologies.

Meanwhile, elemental compositions were analysed by EDS with a detector (XFlash 616, Bruker Nano) attached to the SEM. EDS spectra were acquired at 10 kV to enable detection of elements of carbon, oxygen, sodium and chloride in the polymer matrices. Gold signals from the coating were excluded from the quantitative interpretations.

High-performance liquid chromatography characterizations of the AEHs

The residual monomer contents of the AEHs were analysed using analytical high-performance liquid chromatography (HPLC) (1290II, Agilent) equipped with an XDB-C18 column (4.6 × 150 mm^2, 5 µm bead size). A mixed solution consisting of an aqueous solution of 0.1% (v/v) phosphoric acid and methanol at a ratio of 95:5 (v/v) was used as the mobile phase, extractant and medium. A calibration curve was obtained from the standard AA monomer standard solution diluted with the mobile phase to varying monomer concentrations. To extract the residual monomer from the AEHs, we incubated 2.0 g of each AEH type in 500 ml of the extractant. AEHs of two different ionization degrees (0 and 0.4) and treatments (as-printed and dialysed) were measured. To evaluate the monomer-extraction efficiencies and release profiles, the extracted solutions were collected after 24 h and 72 h. The solution obtained was filtered with a sterile 0.2 µm filter (Millipore Sigma), and a 5 µl sample was injected into the HPLC system for analysis. A mobile phase flow rate of 0.8 ml min^{-1} was used for the tests. The signal intensity as a function of eluting time was measured by a diode array detector at a wavelength of 210 nm. The concentrations of the residual AA monomers in the AEHs were determined based on the calibration curve and converted into the actual concentrations in AEHs.

Mechanical characterizations

The mechanical properties of equilibrium swollen hydrogels were characterized by uniaxial compressive tests using a universal tensile machine (Instron-5967) with a load cell capacity of 100 N.

Compression test. The hydrogel discs (8 × 3 mm^2, diameter × height) of different compositions were soaked in normal saline to allow unconfined swelling to equilibrate for 3 days. Then the swollen samples in equilibrium were tested at room temperature under a compression rate of 50% min^{-1}. Young's modulus was determined by the slope of the stress–strain curve within the 5–10% strain. At least four specimens were measured for each group of samples to obtain the average values.

Tensile test. Rectangular samples of ~0.4 mm in thickness, ~12 mm in length and ~4 mm in width were cut from the film samples for tensile tests. The constant stretching rate was fixed at 50% min^{-1}. Young's modulus was determined by the slope of the stress–strain curve within the 5–10% strain. At least four specimens were measured for each group of samples to obtain the average results.

Adhesion test. The 180° peel test was performed to test the adhesion property of hydrogels. Two pieces of the rabbit skin with a width of 1 cm were prepared. Cured hydrogel film with a thickness of 0.5 mm was placed between the skin pieces and tested at a constant peeling speed of 50% strain per minute. The measured force was recorded to draw the curve.

DLP printer

A custom-built bottom-up DLP printer was designed for 3D/4D printing[68–70]. The printing used UV light engine PRO4500 (Wintech Digital System Technology). The light source, with a resolution of 1,280 × 800 d.p.i. (dots per inch), had a working distance of 92 mm with a maximum exposure field of 65.6 × 41 mm^2. A resin vat consisting of a transparent Teflon film (AF2400, Biogeneral) window was positioned between the light source and the build platform. The build platform on a linear translation stage was controlled by the MATLAB R2020b (MathWorks) code.

The software for this system consisted of two different components, that is, projection and motor control. The projection of the system was handled by the previously defined motherboard that was running a custom MATLAB script. To further enable ease of use, a graphical-user interface was created where the user would define key

inputs. The MATLAB script oversaw establishing the communication with the microcontroller via serial communication to give the commands for the motor movement.

The microcontroller code was written using the Arduino Uno IDE (open-source). This code was responsible for receiving the transmitted data from the motherboard and then communicating these commands to the driver and therefore the motor. To do this, the information had to be read and parsed from serial signal, the parsed data had to then be stored into different variables, and these were then executed by different functions which determine the type, speed and steps of the motor movement.

DLP printing procedures

DLP printing adopted two modes, mono-material printing and multi-material printing.

Mono-material printing. During the bottom-up DLP printing process, the photo-ink was loaded in the resin vat with a transparent window. A gap equal to the printing layer height was initially reserved between the build platform and the bottom of the vat, which would be filled with resin. The digital light controlled by the UV light engine precisely controlled the light patterns for structured photo-curing of hydrogel precursors. The exposure time for each layer was 10–20 s, and the intensity of the exposure area was controlled at 2.6 mW cm^{-2}. The cured slice would be moved up by a distance of one layer thickness with build platform, and the new gap would be filled with the liquid resin. The exposure of the next layer was then performed, which looped through until the entire printed object was completed. To avoid continuous heat accumulation in the resin which adversely affects the shaping accuracy, a cooling time of ~10 s was added between each exposure.

Multi-material printing. Photoinks with different concentrations of PEGDA (M_w = 1,000 g mol^{-1}) were stained by different dyes and maintained in independent resin vats that would be switched during printing. Residual liquid resin was wiped off with dust-free cloth before switching. Considering the light absorption of the visualizing pigments, to ensure similar shaping accuracy when printing different materials, the exposure times of dyed and undyed precursor solutions were 40 s and 20 s, respectively.

3D printing the auricle protheses for in vivo reconstruction. The auricle protheses (length = 6.2 cm, width = 3.3 cm, height = 1.8 cm) in the typical human ear shape and size were printed from a commercial 3D printer (Form 4, FormLabs) using a commercial resin (White Resin V5, FormLabs). Before implantation, these prothesis were immersed in 75% ethanol overnight for sterilization and extensively washed with saline before implantation. The same standard tessellation language (STL) model was used to produce 4D-printed AEH-e-TEs.

Swelling analyses and dialysis treatment

Cast hydrogel discs and printed constructs were weighed and placed into 100 ml of normal saline (0.9% NaCl solution) or DPBS at room temperature. The masses of the swelling hydrogels (n = 4 for each group) were taken at selected time points (1, 2, 3, 4, 5, 6, 8, 10, 12, 14, 16, 18, 24, 36, 48, 72, 96, 120, 144 and 168 h). The swelling ratio was calculated according to equation (1):

$$\text{Swelling ratio} = \frac{m_t}{m_i} \quad (1)$$

where m_t is the mass of the object in the swollen status, and m_i is the mass of the object in initial status before swelling.

For dialysis, hydrogels in the swelling equilibrium were transferred into strong brine (30.0% NaCl solution) for 72 h to allow them to re-shrink. During the shrinkage procedure, the masses of the hydrogels were recorded at selected time points (1, 2, 3, 4, 5, 6, 8, 10, 12, 14, 16, 18, 24, 36, 48 and 72 h). The shrinking ratio was calculated the same as the swelling ratio according to equation (1).

To simulate in vivo metabolism of body fluid, we further established an in vitro fluidic system composed of a set of injection and suction pumps (Supplementary Fig. 9). A pump (right, Lande Medical Equipment) continuously injected DPBS at a rate of 2–10 ml h^{-1}, while the other pump (left, Lead Fluid Intelligent Equipment Manufacturing) withdrew it at a rate of 1–2 ml h^{-1}. We adjusted the reservoir volume (with a maximum capacity of 5–50 ml) and pump speeds according to the sizes of AEH-TEs to ensure the swelling buffer just covered the sample in each experiment. The masses of the hydrogels were recorded at selected time points.

Cellular assay

Cell culture experiments were established by seeding cells into 6-well plates and placing AEH-TE-containing transwell inserts into the wells (Supplementary Fig. 11). HMECs (BDBIO) and HFF-1 cells (BDBIO) at approximately 80% confluence were trypsinized, centrifuged and resuspended in medium. HMECs were seeded at 5×10^5 cells per well, while HFF-1 cells were seeded into each well at a density of 1×10^5 cells per well. The culture media were changed every 2 days. On days 1 and 7, the cells were subjected to live/dead and F-actin staining.

Cell viability was measured by the Live/Dead viability/cytotoxicity kit (Yongqinquan Intelligent Equipment) according to the manufacturer's instructions. Briefly, the attached cells were washed with DPBS twice, followed by the addition of live/dead staining solution containing 4 mM of calcein acetoxymethyl and 2 mM of ethidium homodimer-1 in DPBS (Thermo Fisher Scientific). After incubation at 37 °C for 30 min, the samples were washed three times with DPBS, immersed in the ProLong Live Antifade Reagent (Thermo Fisher Scientific) and observed under a confocal microscope (Leica TCS SP8 CARS). Percentages of viable cells were determined using the ImageJ software 1.53 (National Institutes of Health).

For morphological analyses, the TRITC-Phalloidin kit (Yongqinquan Intelligent Equipment) was used for F-actin staining according to the manufacturer's instructions. The cells were washed with DPBS twice and fixed with 4% (v/v) paraformaldehyde (Sigma-Aldrich) for 10 min. After three times gentle washing, the samples were permeabilized with 0.1% (v/v) Triton X-100 (Sigma-Aldrich) for 10 min at room temperature. Then 200 nM phalloidin (in 0.1% (v/v) BSA, Sigma-Aldrich) was added to each sample and incubated for 30 min at room temperature. The samples were washed again with DPBS and then stained with 4′,6-diamidino-2-phenylindole (DAPI, Sigma-Aldrich) (1:1,000 (v/v) in DPBS) for 10 min at room temperature. The samples were washed with DPBS and immersed in the ProLong Live Antifade Reagent for further observation under a confocal microscope.

MTT assays were conducted via the MTT assay kit (Solarbio). HFF-1 cells and HMECs were seeded into 48-well plates at 5×10^4 and 1×10^4 cells per well, respectively. On day 0, AEH-TEs (α of 0 and 0.4) were soaked in the media for 72 h, which were then used for subsequent cell cultures. The cells cultured in regular media without AEH-TEs were regarded as control groups. Regular media without cells inside was used as the blank groups. On days 1 and 7 of culture, the cells were used for MTT assays. Briefly, the old medium was removed from each well and replaced with 270 µl of fresh medium and 30 µl of MTT solution. After 4 h incubation, 270 µl of formazan dissolution agent was added to each well to replace the reaction medium. After 10 min of gentle shaking, a multimode plate reader (PerkinElmer) was used to read the absorbance values (optical densities) at 490 nm.

Finite element simulation

We used COMSOL Multiphysics to simulate the hygroscopic swelling of an AEH-e-TE (α = 0.4, 1% PEGDA M_w = 1,000) over 72 h through the finite element method. The computer-aided design (CAD) model used for 4D printing was imported, and the material properties, including

Young's modulus (E = 1,116 Pa), the Poisson's ratio (v = 0.15) and the density (ρ = 1,110 kg m^{-3}) were defined. The ear construct was modelled on a flat surface by restricting the displacement of its base along the z direction. The swelling behaviour was simulated by implementing the hygroscopic swelling module of the linear elastic material for membrane physics. The hygroscopic swelling ratio (β_h) was determined experimentally. For discretizing the domain, free triangular meshes with an element size between 0.894 mm and 4.97 mm, a maximum growth rate of 1.5 and a curvature factor of 0.6 were used. We conducted the simulation using a time-dependent study with a time step of 1 h and a range of 72 h, which is experimentally sufficient to reach a plateau for swelling.

In vivo implantation and explanation

New Zealand white rabbits were selected as the animal model because of their extensive similarity with the human skin than other large-animal models. Animal experiments were approved by the Animal Care and Experiment Committee (Approval Number, 2023animal(98)) of Plastic Surgery Hospital, Chinese Academy of Medical Sciences & Peking Union Medical College. Female New Zealand white rabbits weighing 2.5–3.0 kg and 5–6 months old (n = 24) were housed in an environment with a temperature of 22 ± 1 °C and a relative humidity of 50 ± 1%.

For comparisons between the AEH-TEs and NVP–MMA tissue expanders, they were implanted into rabbits under the skin of their hypochondrium (Supplementary Videos 7, 8 and 11). The hypochondrium was selected to simulate the clinically relevant hard region of the human body. The anatomical location, body fluid environment, flap thickness and tissue layers of the hypochondrium are highly similar to those of the postauricular mastoid area for AEH-e-TE-implantation and the chest area for AEH-b-TE-implantation in clinical applications.

In stage I, diluted lidocaine solution was injected to bluntly dissect, followed by incision and undermining of the skin. After implantation of the hydrogel, the incision was closed by suturing. For evaluating the AEH-e-TEs, in an additional stage II procedure, the skin was cut at the original incision. The expanded pocket was irrigated by normal saline after explantation of the expanded implant. Then, a 3D-printed auricle prothesis was inserted into the pocket, and the incision was closed. Finally, negative pressure suction was performed to generate a distinguishable human auricle shape by a 20 ml syringe and a 10 cm blunt needle.

For further comparisons with the kidney-shaped silicone tissue expanders, we performed similar stage I and stage II operations as described above. Differently, before insertion of the silicone tissue expander, we had to test its leak-proofness by injection of air. Moreover, one additional tunnel needed to be undermined to place the injection port as well as the connector tube. Another suture outside the skin was made to fix the connector tube and the injection port. Before the stage II surgery, we injected 5 or 10 ml normal saline daily into the silicone tissue expander through the injection port. In stage III (flap-trimming operation), the removal area was first marked, followed by incision and removal of marked skin tissue. This long incision was finally closed by suture (Supplementary Video 10).

The haematoma model was established by cutting off two visible subdermal blood vessels without haemostasis after dissection and undermining. The implanted AEH-e-TEs were explanted on day 7 or day 14 and weighed.

CT scanning and 3D reconstruction of implanted AEH-e-TEs

Post-surgical rabbits were anaesthetized and scanned using a CT scanner (Philips Healthcare) to collect digital images at days 3, 7 and 14, which were transferred to a 3D software (Mimics 21.0 and 3-Matic 14.0, Materialise) for reconstruction. The reconstructed 3D data were used for measuring the expanded skins area using the same 3D software.

Systemic inflammation assessments and histological staining

At days 1, 3, 7 and 14, venous blood was collected through the marginal ear vein of the rabbit. Whole blood sample (50 µl) from each rabbit was added into a haematology analyser (HF-3800, HLIFE, HKANGYU) for counting. The expressions of inflammatory biomarkers were determined using ELISA kits (Medical Discovery Leader). The assays were performed following the manufacturer's instructions, and each sample was assayed twice.

After the removal of AEH-e-TEs on day 14, the expanded areas and un-expanded areas of the skins were both collected and fixed in formalin (Thermo Fisher Scientific) for 24 h for histological staining. The fixed specimens were then embedded in paraffin and cut into 5 µm slices. Masson's trichrome staining was performed according to the manufacturer's instruction (Solarbio Science & Technology). Immunofluorescence staining was performed using an anti-PCNA antibody (Proteintech) for the detection of proliferating cells and anti-CD34 antibody (Invitrogen) for detecting tissue vascularization. After the tissue sections were deparaffinized and rehydrated, they were incubated with either one of the primary antibodies overnight at 4 °C. These antigens were visualized with a fluorescein isothiocyanate-conjugated secondary antibody (Thermo Fisher Scientific). The nuclei were counterstained with 0.1 mg ml^{-1} of DAPI. Stained sections were observed under an Eclipse Ti2 inverted microscope (Nikon). The proliferative cells were counted as the number of PCNA-positive (PCNA$^+$) cells per area (300 × 300 µm^2).

Statistical analyses

All the experiments were conducted in triplicates to quintuples for each data point and were repeated three to four times. Results were expressed as means ± standard errors of the means of three or four independent experiments, and statistical comparisons were performed using the t-test and the one-way analysis of variance test. $P < 0.05$ was considered statistically significant.

Reporting summary

Further information on research design is available in the Nature Portfolio Reporting Summary linked to this article.

Data availability

All data needed to evaluate the conclusions in the paper are included in the Article and/or Supplementary Information. Source data are provided with this paper.

References

1. Finnerty, C. C. et al. Hypertrophic scarring: the greatest unmet challenge after burn injury. *Lancet* **388**, 1427–1436 (2016).
2. Lee, G. K. & Sheckter, C. C. Breast reconstruction following breast cancer treatment—2018. *JAMA* **320**, 1277–1278 (2018).
3. Zhou, G. et al. In vitro regeneration of patient-specific ear-shaped cartilage and its first clinical application for auricular reconstruction. *EBioMedicine* **28**, 287–302 (2018).
4. Vergier, B. et al. Proliferative nodules vs melanoma arising in giant congenital melanocytic nevi during childhood. *JAMA Dermatol.* **152**, 1147–1151 (2016).
5. Li, M. L. Rhinoplasty. *JAMA Otolaryngol. Head Neck Surg.* **148**, 1188 (2022).
6. Lee, J. W. et al. Auricular reconstruction for bilateral auricular deformity caused by relapsing polychondritis. *JAMA Otolaryngol. Head Neck Surg.* **149**, 94–95 (2023).
7. Radovan, C. Tissue expansion in soft-tissue reconstruction. *Plast. Reconstr. Surg.* **74**, 482–492 (1984).
8. Guo, Y. et al. Mechanical stretch induced skin regeneration: molecular and cellular mechanism in skin soft tissue expansion. *Int. J. Mol. Sci.* **23**, 9622 (2022).

9. Zhu, H. et al. Application of tissue expansion with perforator flaps for reconstruction of challenging skin lesions. *J. Reconstr. Microsurg.* **34**, 13–20 (2018).
10. Aragona, M. et al. Mechanisms of stretch-mediated skin expansion at single-cell resolution. *Nature* **584**, 268–273 (2020).
11. LeGoff, L. & Lecuit, T. Mechanical forces and growth in animal tissues. *Cold Spring Harb. Perspect. Biol.* **8**, a019232 (2015).
12. Zöllner, A. M., Holland, M. A., Honda, K. S., Gosain, A. K. & Kuhl, E. Growth on demand: reviewing the mechanobiology of stretched skin. *J. Mech. Behav. Biomed. Mater.* **28**, 495–509 (2013).
13. Pallua, N. & von Heimburg, D. Pre-expanded ultra-thin supraclavicular flaps for (full-) face reconstruction with reduced donor-site morbidity and without the need for microsurgery. *Plast. Reconstr. Surg.* **115**, 1837–1844 (2005). discussion 1845-1837.
14. Cordeiro, P. G. Breast reconstruction after surgery for breast cancer. *New Engl. J. Med.* **359**, 1590–1601 (2008).
15. Braun, T. L. et al. Tissue expansion in children. *Semin. Plast. Surg.* **30**, 155–161 (2016).
16. Neumann, C. G. The expansion of an area of skin by progressive distention of a subcutaneous balloon; use of the method for securing skin for subtotal reconstruction of the ear. *Plast. Reconstr. Surg.* **19**, 124–130 (1957).
17. Pan, B. et al. Microtia: ear reconstruction using tissue expander and autogenous costal cartilage. *J. Plast. Reconstr. Aesthet. Surg.* **61**, S98–S103 (2008).
18. Wiese, K. G. Osmotically induced tissue expansion with hydrogels: a new dimension in tissue expansion? A preliminary report. *J. Craniomaxillofac. Surg.* **21**, 309–313 (1993).
19. Hrib, J. et al. Hydrogel tissue expanders for stomatology. Part II. Poly(styrene-maleic anhydride) hydrogels. *Polymers* **11**, 1087 (2019).
20. Chummun, S., Addison, P. & Stewart, K. J. The osmotic tissue expander: a 5-year experience. *J. Plast. Reconstr. Aesthet. Surg.* **63**, 2128–2132 (2010).
21. Wiese, K. G., Heinemann, D. E., Ostermeier, D. & Peters, J. H. Biomaterial properties and biocompatibility in cell culture of a novel self-inflating hydrogel tissue expander. *J. Biomed. Mater. Res.* **54**, 179–188 (2001).
22. Swan, M. C., Bucknall, D. G., Goodacre, T. E. & Czernuszka, J. T. Synthesis and properties of a novel anisotropic self-inflating hydrogel tissue expander. *Acta Biomater.* **7**, 1126–1132 (2011).
23. Jamadi, M. et al. Poly (ethylene glycol)-based hydrogels as self-inflating tissue expanders with tunable mechanical and swelling properties. *Macromol. Biosci.* **17**, 1600479 (2017).
24. Gong, J. P., Katsuyama, Y., Kurokawa, T. & Osada, Y. Double-network hydrogels with extremely high mechanical strength. *Adv. Mater.* **15**, 1155–1158 (2003).
25. Sun, J. Y. et al. Highly stretchable and tough hydrogels. *Nature* **489**, 133–136 (2012).
26. Kim, J., Zhang, G., Shi, M. & Suo, Z. Fracture, fatigue, and friction of polymers in which entanglements greatly outnumber cross-links. *Science* **374**, 212–216 (2021).
27. Li, X. et al. Mesoscale bicontinuous networks in self-healing hydrogels delay fatigue fracture. *Proc. Natl Acad. Sci. USA* **117**, 7606–7612 (2020).
28. Li, X. et al. Effect of mesoscale phase contrast on fatigue-delaying behavior of self-healing hydrogels. *Sci. Adv.* **7**, eabe8210 (2021).
29. Serra, L., Doménech, J. & Peppas, N. A. Drug transport mechanisms and release kinetics from molecularly designed poly(acrylic acid-g-ethylene glycol) hydrogels. *Biomaterials* **27**, 5440–5451 (2006).
30. Browe, D. P. et al. Characterization and optimization of actuating poly(ethylene glycol) diacrylate/acrylic acid hydrogels as artificial muscles. *Polymer* **117**, 331–341 (2017).
31. Ozcelik, B. et al. Highly porous and mechanically robust polyester poly(ethylene glycol) sponges as implantable scaffolds. *Acta Biomater.* **10**, 2769–2780 (2014).
32. Mintis, D. G. & Mavrantzas, V. G. Effect of pH and molecular length on the structure and dynamics of short poly(acrylic acid) in dilute solution: detailed molecular dynamics study. *J. Phys. Chem. B* **123**, 4204–4219 (2019).
33. Richbourg, N. R. & Peppas, N. A. The swollen polymer network hypothesis: quantitative models of hydrogel swelling, stiffness, and solute transport. *Prog. Polym. Sci.* **105**, 101243 (2020).
34. Jia, D. & Muthukumar, M. Theory of charged gels: swelling, elasticity, and dynamics. *Gels* **7**, 49 (2021).
35. Mazzoccoli, J. P., Feke, D. L., Baskaran, H. & Pintauro, P. N. Mechanical and cell viability properties of crosslinked low- and high-molecular weight poly(ethylene glycol) diacrylate blends. *J. Biomed. Mater. Res. A* **93**, 558–566 (2010).
36. Wu, Z. L. et al. Three-dimensional shape transformations of hydrogel sheets induced by small-scale modulation of internal stresses. *Nat. Commun.* **4**, 1586 (2013).
37. Pati, F. et al. Printing three-dimensional tissue analogues with decellularized extracellular matrix bioink. *Nat. Commun.* **5**, 3935 (2014).
38. Wang, D. et al. Microfluidic bioprinting of tough hydrogel-based vascular conduits for functional blood vessels. *Sci. Adv.* **8**, eabq6900 (2022).
39. Bartel-Friedrich, S. Congenital auricular malformations: description of anomalies and syndromes. *Facial Plast. Surg.* **31**, 567–580 (2015).
40. Luquetti, D. V., Leoncini, E. & Mastroiacovo, P. Microtia-anotia: a global review of prevalence rates. *Birth Defects Res. A* **91**, 813–822 (2011).
41. Zhang, Y. et al. Microtia in a Chinese specialty clinic population: clinical heterogeneity and associated congenital anomalies. *Plast. Reconstr. Surg.* **142**, 892e–903e (2018).
42. Chen, X. et al. Microtia part I: preoperation and in-operation lessons from 1012 ear reconstruction operations. *Aesthetic Plast. Surg.* **46**, 2781–2787 (2022).
43. Hata, Y., Hosokawa, K., Yano, K., Matsuka, K. & Ito, O. Correction of congenital microtia using the tissue expander. *Plast. Reconstr. Surg.* **84**, 741–751 (1989). discussion 752-743.
44. Park, C. Subfascial expansion and expanded two-flap method for microtia reconstruction. *Plast. Reconstr. Surg.* **106**, 1473–1487 (2000).
45. Karimi, H. et al. Tissue expanders; review of indications, results and outcome during 15 years' experience. *Burns* **45**, 990–1004 (2019).
46. Shibahara, K. -i & Stillman, B. Replication-dependent marking of DNA by PCNA facilitates CAF-1-coupled inheritance of chromatin. *Cell* **96**, 575–585 (1999).
47. Chung, L. et al. Interleukin 17 and senescent cells regulate the foreign body response to synthetic material implants in mice and humans. *Sci. Transl. Med.* **12**, eaax3799 (2020).
48. Leineweber, C., Müller, E. & Marschang, R. E. Blood reference intervals for rabbits (*Oryctolagus cuniculus*) from routine diagnostic samples. *Tierarztl. Prax. Ausg. K Kleintiere Heimtiere* **46**, 393–398 (2018).
49. Said, S. et al. Genetic analysis of over half a million people characterises C-reactive protein loci. *Nat. Commun.* **13**, 2198 (2022).
50. Silva, M. M. et al. Systemic Inflammatory reaction after silicone breast implant. *Aesthetic Plast. Surg.* **35**, 789–794 (2011).
51. Smole, U. et al. Serum amyloid A is a soluble pattern recognition receptor that drives type 2 immunity. *Nat. Immunol.* **21**, 756–765 (2020).

52. Broderick, L. & Hoffman, H. M. IL-1 and autoinflammatory disease: biology, pathogenesis and therapeutic targeting. *Nat. Rev. Rheumatol.* **18**, 448–463 (2022).
53. Swan, M. C., Bucknall, D. G., Czernuszka, J. T., Pigott, D. W. & Goodacre, T. E. Development of a novel anisotropic self-inflating tissue expander: in vivo submucoperiosteal performance in the porcine hard palate. *Plast. Reconstr. Surg.* **129**, 79–88 (2012).
54. Ma, L. et al. Stepwise self-inflating hydrogel expansion for congenital anophthalmia and blind microphthalmia: over 15 years' experience in China. *J. Plast. Reconstr. Aesthet. Surg.* **90**, 40–46 (2024).
55. Ellesøe, A. G., Shado, R., Pereira, I. N., Madruga, D. & Hassan, H. Soft tissue expansion using self-inflating osmotic hydrogel expanders prior to bone augmentation: healing and complications. Evidence-based review. *BDJ Open* **9**, 48 (2023).
56. De La Cruz Monroy, M. F. I., Kalaskar, D. M. & Rauf, K. G. Tissue expansion reconstruction of head and neck burn injuries in paediatric patients - a systematic review. *JPRAS Open* **18**, 78–97 (2018).
57. Jing, C. & Hong-Xing, Z. Partial necrosis of expanding postauricular flaps during auricle reconstruction: risk factors and effective management. *Plast. Reconstr. Surg.* **119**, 1759–1766 (2007).
58. Kabaker, S. B. An update on tissue expansion in head and neck surgery. *Arch. Otolaryngol. Head Neck Surg.* **116**, 152–153 (1990).
59. De Brito Henriques, J. G., Filho, G. P., Gusmão, S. N., Henriques, K. S. & Miranda, M. E. Intraoperative acute tissue expansion for the closure of large myelomeningoceles. *J. Neurosurg.* **107**, 98–102 (2007).
60. Zopf, D. A., Knecht, E. & Kim, J. in *Cummings Pediatric Otolaryngology* 2nd edn (ed. Lesperance, M. M.) 249-258 (Elsevier, 2021).
61. Jiang, H., Pan, B., Lin, L., Cai, Z. & Zhuang, H. Ten-year experience in microtia reconstruction using tissue expander and autogenous cartilage. *Int. J. Pediatr. Otorhinolaryngol.* **72**, 1251–1259 (2008).
62. Levato, R. et al. Light-based vat-polymerization bioprinting. *Nat. Rev. Methods Primers* **3**, 47 (2023).
63. Heinrich, M. A. et al. 3D bioprinting: from benches to translational applications. *Small* **15**, e1805510 (2019).
64. Wang, D. et al. Extrusion bioprinting of elastin-containing bioactive double-network tough hydrogels for complex elastic tissue regeneration. *Aggregate* **00**, e477 (2024).
65. Azzi, J. L., Thabet, C., Azzi, A. J. & Gilardino, M. S. Complications of tissue expansion in the head and neck. *Head Neck* **42**, 747–762 (2020).
66. McCarthy, C. M., Disa, J. J., Pusic, A. L., Mehrara, B. J. & Cordeiro, P. G. The effect of closed-suction drains on the incidence of local wound complications following tissue expander/implant reconstruction: a cohort study. *Plast. Reconstr. Surg.* **119**, 2018–2022 (2007).
67. Tsoi, B. et al. Safety of tissue expander/implant versus autologous abdominal tissue breast reconstruction in postmastectomy breast cancer patients: a systematic review and meta-analysis. *Plast. Reconstr. Surg.* **133**, 234–249 (2014).
68. Wang, M. et al. Digital light processing based bioprinting with composable gradients. *Adv. Mater.* **34**, e2107038 (2022).
69. Liao, J. et al. 3D-printable colloidal photonic crystals. *Mater. Today* **56**, 29–41 (2022).
70. Wang, M. et al. Molecularly cleavable bioinks facilitate high-performance digital light processing-based bioprinting of functional volumetric soft tissues. *Nat. Commun.* **13**, 3317 (2022).

Acknowledgements

Support from the Brigham Research Institute Ministry of Science and ICT is acknowledged. D.W. further acknowledges the National Natural Science Foundation of China (82402936) for partial support. We appreciate the valuable suggestion from S. Zhan from the Clinical Laboratory of Plastic Surgery Hospital of Chinese Academy of Medical Sciences & Peking Union Medical College.

Author contributions

Y.S.Z., D.W. and X.K. conceived the idea. D.W., J.-Q.L., J.-S.L., C.E.G-M. and P.A. set up the printing system and participated in printing experiments. X.K. and H.R. performed simulation and theoretical analyses. D.W., J.-Q.L., L.L., J.-S.L., S.Y., G.T. and M.X. performed swelling tests and characterization experiments. D.W., W.C. and H.J. designed and performed animal experiments. Z.W., X.K. and D.W. designed the scheme and illustrations. S.M. contributed to methods for additional key experimental designs. D.W., J.-S.L., X.K., H.J. and Y.S.Z. wrote the paper, and all authors reviewed the manuscript. Y.S.Z. and H.J. supervised the project.

Competing interests

Y.S.Z. consulted for Allevi by 3D Systems; consults for PepGel; cofounded, consults for and holds options of Linton Lifesciences and Criocore; and sits on the scientific advisory board and holds options of Xellar Biosystems. The relevant interests are managed by the Brigham and Women's Hospital. The other authors declare no competing interests.

Additional information

Supplementary information The online version contains supplementary material available at https://doi.org/10.1038/s41551-026-01681-z.

Correspondence and requests for materials should be addressed to Haiyue Jiang or Yu Shrike Zhang.

Peer review information *Nature Biomedical Engineering* thanks Dong-Woo Cho, Michael Gelinsky and the other, anonymous, reviewer(s) for their contribution to the peer review of this work.

nature portfolio

Corresponding author(s): Yu Shrike Zhang

Last updated by author(s): Jul 24, 2025

Reporting Summary

Nature Portfolio wishes to improve the reproducibility of the work that we publish. This form provides structure for consistency and transparency in reporting. For further information on Nature Portfolio policies, see our Editorial Policies and the Editorial Policy Checklist.

Statistics

For all statistical analyses, confirm that the following items are present in the figure legend, table legend, main text, or Methods section.

n/a	Confirmed	
☐	☒	The exact sample size (*n*) for each experimental group/condition, given as a discrete number and unit of measurement
☐	☒	A statement on whether measurements were taken from distinct samples or whether the same sample was measured repeatedly
☐	☒	The statistical test(s) used AND whether they are one- or two-sided *Only common tests should be described solely by name; describe more complex techniques in the Methods section.*
☒	☐	A description of all covariates tested
☒	☐	A description of any assumptions or corrections, such as tests of normality and adjustment for multiple comparisons
☐	☒	A full description of the statistical parameters including central tendency (e.g. means) or other basic estimates (e.g. regression coefficient) AND variation (e.g. standard deviation) or associated estimates of uncertainty (e.g. confidence intervals)
☐	☒	For null hypothesis testing, the test statistic (e.g. *F*, *t*, *r*) with confidence intervals, effect sizes, degrees of freedom and *P* value noted *Give P values as exact values whenever suitable.*
☒	☐	For Bayesian analysis, information on the choice of priors and Markov chain Monte Carlo settings
☒	☐	For hierarchical and complex designs, identification of the appropriate level for tests and full reporting of outcomes
☒	☐	Estimates of effect sizes (e.g. Cohen's *d*, Pearson's *r*), indicating how they were calculated

Our web collection on statistics for biologists contains articles on many of the points above.

Software and code

Policy information about availability of computer code

Data collection	N/A
Data analysis	Images processed and quantified using ImageJ software, Graphs plotted using Graphpad Prism 8 software, 3D data and images processed using Mimics and 3-Matic software.

For manuscripts utilizing custom algorithms or software that are central to the research but not yet described in published literature, software must be made available to editors and reviewers. We strongly encourage code deposition in a community repository (e.g. GitHub). See the Nature Portfolio guidelines for submitting code & software for further information.

Data

Policy information about availability of data

All manuscripts must include a data availability statement. This statement should provide the following information, where applicable:

- Accession codes, unique identifiers, or web links for publicly available datasets
- A description of any restrictions on data availability
- For clinical datasets or third party data, please ensure that the statement adheres to our policy

The relevant data generated in this study are provided in the Supplementary Information. Additional datasets are available from the lead contact upon reasonable requests. This paper does not report original code.

Research involving human participants, their data, or biological material

Policy information about studies with human participants or human data. See also policy information about sex, gender (identity/presentation), and sexual orientation and race, ethnicity and racism.

Reporting on sex and gender	*Use the terms sex (biological attribute) and gender (shaped by social and cultural circumstances) carefully in order to avoid confusing both terms. Indicate if findings apply to only one sex or gender; describe whether sex and gender were considered in study design; whether sex and/or gender was determined based on self-reporting or assigned and methods used.* *Provide in the source data disaggregated sex and gender data, where this information has been collected, and if consent has been obtained for sharing of individual-level data; provide overall numbers in this Reporting Summary. Please state if this information has not been collected.* *Report sex- and gender-based analyses where performed, justify reasons for lack of sex- and gender-based analysis.*
Reporting on race, ethnicity, or other socially relevant groupings	*Please specify the socially constructed or socially relevant categorization variable(s) used in your manuscript and explain why they were used. Please note that such variables should not be used as proxies for other socially constructed/relevant variables (for example, race or ethnicity should not be used as a proxy for socioeconomic status).* *Provide clear definitions of the relevant terms used, how they were provided (by the participants/respondents, the researchers, or third parties), and the method(s) used to classify people into the different categories (e.g. self-report, census or administrative data, social media data, etc.)* *Please provide details about how you controlled for confounding variables in your analyses.*
Population characteristics	*Describe the covariate-relevant population characteristics of the human research participants (e.g. age, genotypic information, past and current diagnosis and treatment categories). If you filled out the behavioural & social sciences study design questions and have nothing to add here, write "See above."*
Recruitment	*Describe how participants were recruited. Outline any potential self-selection bias or other biases that may be present and how these are likely to impact results.*
Ethics oversight	*Identify the organization(s) that approved the study protocol.*

Note that full information on the approval of the study protocol must also be provided in the manuscript.

Field-specific reporting

Please select the one below that is the best fit for your research. If you are not sure, read the appropriate sections before making your selection.

☒ Life sciences ☐ Behavioural & social sciences ☐ Ecological, evolutionary & environmental sciences

For a reference copy of the document with all sections, see nature.com/documents/nr-reporting-summary-flat.pdf

Life sciences study design

All studies must disclose on these points even when the disclosure is negative.

Sample size	Sample size was not predetermined, and was selected upon reasonable standard sample size for in vivo studies. Multiple repetition of the experiments resulted in comparable results. n value greater than the least number is reported and exact n value can be provided.
Data exclusions	No datasets were excluded.
Replication	All experiments were highly reproducible. The results were reproduced at least three times and verified with in vivo studies.
Randomization	We randomly allocated rabbits into different groups to receive different implants.
Blinding	Blinded investigators that are not aware of the experimental information were involved in group allocation.

Reporting for specific materials, systems and methods

We require information from authors about some types of materials, experimental systems and methods used in many studies. Here, indicate whether each material, system or method listed is relevant to your study. If you are not sure if a list item applies to your research, read the appropriate section before selecting a response.

Materials & experimental systems

n/a	Involved in the study
☐	☒ Antibodies
☐	☒ Eukaryotic cell lines
☒	☐ Palaeontology and archaeology
☐	☒ Animals and other organisms
☒	☐ Clinical data
☒	☐ Dual use research of concern
☒	☐ Plants

Methods

n/a	Involved in the study
☒	☐ ChIP-seq
☒	☐ Flow cytometry
☒	☐ MRI-based neuroimaging

Antibodies

Antibodies used: PCNA Monoclonal antibody (Proteintech, Rosemont, IL, USA, Cat No. 60097-1-Ig, Clone No.10D10E11, Lot No. 10003678)
CD34 Monoclonal Antibody (Invitrogen, Carlsbad, CA, USA, Cat No. MA1-22646, Clone No. MEC14.7, Lot No.XH3683401)

Validation: All primary antibodies were validated by the manufacturer.

Eukaryotic cell lines

Policy information about cell lines and Sex and Gender in Research

Cell line source(s): Human mammary epithelial cells (HMECs, BDBIO, Hangzhou, China)
Human foreskin fibroblasts-1 (HFF-1, BDBIO, Hangzhou, China)

Authentication: Cell line was authenticated by the manufacturer.

Mycoplasma contamination: Mycoplasma contamination is assumed to be checked by the manufacturer.

Commonly misidentified lines (See ICLAC register): N/A

Animals and other research organisms

Policy information about studies involving animals; ARRIVE guidelines recommended for reporting animal research, and Sex and Gender in Research

Laboratory animals: Female New Zealand white rabbits weighing 2.5–3.0 kg.

Wild animals: This study did not involve wild animals.

Reporting on sex: The findings reported in this study does not apply to only one sex. However, we have unified the sex of rabbits as female for the ease and precisely controlled experimental results since female rabbits are less aggressive. Male rabbits are more active and likely to damage the implants by hitting the cage on purpose.

Field-collected samples: This study did not involve samples collected from the field.

Ethics oversight: Animal experiments were approved by the Animal Care and Experiment Committee (Approval Number, 2023animal(98)) of Plastic Surgery Hospital, Chinese Academy of Medical Sciences & Peking Union Medical College.

Note that full information on the approval of the study protocol must also be provided in the manuscript.

Plants

Seed stocks: *Report on the source of all seed stocks or other plant material used. If applicable, state the seed stock centre and catalogue number. If plant specimens were collected from the field, describe the collection location, date and sampling procedures.*

Novel plant genotypes: *Describe the methods by which all novel plant genotypes were produced. This includes those generated by transgenic approaches, gene editing, chemical/radiation-based mutagenesis and hybridization. For transgenic lines, describe the transformation method, the number of independent lines analyzed and the generation upon which experiments were performed. For gene-edited lines, describe the editor used, the endogenous sequence targeted for editing, the targeting guide RNA sequence (if applicable) and how the editor was applied.*

Authentication: *Describe any authentication procedures for each seed stock used or novel genotype generated. Describe any experiments used to assess the effect of a mutation and, where applicable, how potential secondary effects (e.g. second site T-DNA insertions, mosiacism, off-target gene editing) were examined.*